UNIVERSITAT POLITÈCNICA DE VALÈNCIA

Escuela Técnica Superior de Ingeniería del Diseño

máster en ingeniería mecatrónica

POLYTECHNIC UNIVERSITY OF VALENCIA

SCHOOL OF DESIGN ENGINEERING

MASTER'S DEGREE IN MECHATRONICS ENGINEERING

CONTROL SYSTEM DESIGN FOR A HIGH PERFORMANCE IN A HORIZONTAL TWO-AXIS ROBOT ARM

Nagoya Institute of Technology

Authors:
ALVARO BURCIO CRESPO
ULISES GUILLERMO MOLINA MONTALVÁN

Supervisor:
MAKOTO IWASAKI

JULY 2017

Acknowledgment

Thanks to our supervisor Makoto Iwasaki for giving us the opportunity to do a research period at Nagoya Institute of Technology. As well as the teachers and students belonging to the Mechanical and Electrical Department from Nagoya Institute of Technology and also Denso Corporation for providing the necessary equipment.

Abstract

In this research, tasks of I+D+i for companies in the automotive industrial sector were performed. The equipment under test was a simplification of a 4-Axis SCARA robot from Denso Company. The prismatic and the rotation link, destined to the tool, were removed from the robot making in a 2-Axis robot. In this equipment were developed and implemented several controllers which suppressed the fundamental frequencies, produced by the physical construction of the robot, in order to achieve an improvement in work efficiency and productivity of the production lines. These different typologies of control provided higher speed and higher accuracy in the positioning, in order to accomplish the client specifications, Denso Corporation.

Contents

1 Introduction **1**
1.1 Background of this research . . . 2
1.2 Purpose of this research . . . 2
1.3 Structure of this thesis . . . 3

2 Description of the EUT **4**
2.1 Equipment Under Test Configuration . . . 5
2.1.1 Simplified *SCARA* Robot (2 axes) . . . 5
2.1.2 Joint actuator specifications . . . 6
2.1.3 P-PI DENSO Controller . . . 6
2.2 *Harmonic Drive Gear* . . . 7
2.2.1 HDG Characteristics. Structure and operation principle of the Harmonic Drive Gear . . . 7
2.2.2 Nonlinear characteristics of wave gear . . . 8
2.2.3 Modelling Non-Linearities friction characteristics . . . 9

3 Mathematical Model **14**
3.1 Introduction . . . 15
3.2 Sine Sweep . . . 15
3.2.1 Experiments Characteristics . . . 15
3.2.2 Experiment Results . . . 16
3.3 Previous Mathematical Model . . . 17
3.3.1 Construction of Numerical Simulator . . . 17
3.3.2 Building a mathematical model . . . 17
3.4 New Identified Mathematical Model . . . 19
3.4.1 Preamble . . . 19
3.4.2 Matlab Ident Tool . . . 19
3.4.3 Fitting Identification . . . 21
3.5 Mathematical Models Comparison . . . 23
3.6 Mathematical Models Conclusions . . . 24

4 Reference and Time Response **29**
4.1 Introduction . . . 30
4.2 Reference Characteristics . . . 30
4.3 Angle Reference Test . . . 30
4.4 Time Response Angle Reference. Verification of actual machine response reproducibility by simulator . . . 31
4.5 Experiments Determination . . . 32

5 Controllers Development **37**
5.1 Preliminary . . . 38
5.1.1 Performance Requirements . . . 38
5.1.2 Experiments 1 & 2 . . . 38
5.1.3 Starting Point. P-PI Denso Controller. Feedback Gain Design of Control System . . . 38
5.2 1 DOF Semiclosed . . . 38
5.3 1 DOF Fullclosed . . . 39
5.4 2 DOF Semiclosed. Feedforward compensator based on irreducible decomposition expression . . . 40
5.5 2 DOF Fullclosed . . . 45
5.6 Lead Compensator . . . 47
5.7 Comparison . . . 51

6 Inter-axis Interference Force **57**
6.1 Introduction . . . 58
6.2 Comparison Time Response Experiments . . . 59

7 Disturbance Testing Simulation **62**
7.1 Disturbance . . . 63
7.2 Lead Compensator with Disturbance . . . 63
7.3 Lead Lag Compensator . . . 64
7.4 Time Response with Disturbance . . . 67

8 Conclusion **69**
8.1 Conclusions . . . 70
8.2 Future Tasks . . . 70

Referencess **71**

A Sine Sweep Frequency for an Adaptive Controller **72**

B Interaction between J1 & J2 **74**

C Flowchart to design a controller based in the root locus **83**

List of Tables

2.1 First axis Drive Actuator (FHA-11C-100) Specifications 7
2.2 Second axis Drive Actuator (FHA-8C-100) Specifications 8
2.3 Control system gain 8
2.4 Transition during driving of HDG 10
2.5 Result of friction parameter identification on the first axis 11
2.6 Result of friction parameter identification on the second axis 12

3.1 Sine sweep measurement condition 15
3.2 First axis motor side plant frequency characteristics 18
3.3 First axis load side plant frequency characteristics 19
3.4 Second axis motor side plant frequency characteristics 20
3.5 Second axis load side plant frequency characteristics 21
3.6 Summarise of Math. Model Conclusions 24

4.1 Angles test results 31

5.1 Comparison between experiments and simulations 1 DOF semi-closed control system 42
5.2 Comparison between experiments and simulations 1 DOF full-closed control system 42
5.3 Comparison between experiments and simulations 2 DOF semi-closed control system 45
5.4 Comparison between experiments and simulations 2 DOF semi-closed control system 46
5.5 Lead Compensator Simulation Characteristics 53

List of Figures

2.1 Equipment Under Test 5
2.2 Schematic diagram of the EUT 6
2.3 Schematic diagram of the Encoder 6
2.4 Scheme of Plant Model differentiation. Motor and Load 7
2.5 Actual machine control system block diagram 7
2.6 HDG Overview [Cat, 2004] 9
2.7 Concept of friction characteristics 11
2.8 Results of modelling friction characteristics on first axis 12
2.9 Results of modelling friction characteristics on second axis 13

3.1 Control system block diagram at frequency characteristic measurement 16
3.2 Frequency characteristics of the first axis of a bi-axial $SCARA$ robot 16
3.3 Frequency characteristics of the second axis of a bi-axial $SCARA$ robot . . . 17
3.4 Frequency characteristic model from the torque command to the motor position on the first axis 18
3.5 Frequency characteristic model from the torque command to the load position on the first axis 19
3.6 Frequency characteristic model from the torque command to the motor position on the second axis 20
3.7 Frequency characteristic model from the torque command to the load position on the second axis 21
3.8 Identified Mathematical Model with Ident Tool Function 22
3.9 First Fitting: Global Actuator Behaviour $G_1(s)$ 23
3.10 Second and Third Fitting 24
3.11 Fitting result $G(s)$ 25
3.12 Transfer function bode diagram in the fitting behaviour at low frequencies $G_{lf}(s)$ 26
3.13 Fitting Result Improved $G^*(s)$ 26
3.14 Joint 1 & 2, motor and load fitting identification 27
3.15 Comparison between previous and new identified mathematical model 28

4.1 Reference waveform, Acceleration, Velocity and Position 31
4.2 Acceleration, Velocity and Position Reference to 3 Degrees 32
4.3 First axis motor position response reproducibility 33

4.4 First axis load position response reproducibility 34
4.5 First axis Torque Command reproducibility 34
4.6 Second axis motor position response reproducibility 35
4.7 Second axis load position response reproducibility 35
4.8 Second axis Torque Command reproducibility 36

5.1 Block Diagram of 1DOF Semi-closed Control System 39
5.2 Experimental results (0 to 3° [load deg]) by the first-axis 1DOF semi-closed control system 40
5.3 Experimental results (0 to 3° [load deg]) by the second-axis 1DOF semi-closed control system 41
5.4 Block Diagram of 1DOF Full-closed Control System 42
5.5 Experimental results (0 to 3° [load deg]) by the first-axis 1DOF full-closed control system 43
5.6 Experimental results (0 to 3° [load deg]) by the second-axis 1DOF full-closed control system 44
5.7 Block Diagram of 2DOF Semi-closed Control System applying FF compensator based on irreducible decomposition 45
5.8 Transmission characteristic of the feedforward compensator of the first axis (semi-closed control system) 46
5.9 Transmission characteristic of the feedforward compensator of the second axis (semi-closed control system) 47
5.10 Experimental results (0 to 3° [load deg]) by the first-axis 2DOF semi-closed control system 48
5.11 Experimental results (0 to 3° [load deg]) by the second-axis 2DOF semi-closed control system 49
5.12 Block Diagram of 2DOF Full-closed Control System applying FF compensator based on irreducible decomposition 50
5.13 Experimental results (0 to 3° [load deg]) by the first-axis 2DOF full-closed control system 51
5.14 Experimental results (0 to 3° [load deg]) by the second-axis 2DOF full-closed control system 52
5.15 Block Diagram of the Lead Compensator 53
5.16 Lead Compensator Bode Diagram 53
5.17 Comparison of simulation results (0 to 3° [load deg])by the first-axis between the different controllers and the Lead Compensator 54
5.18 Comparison of simulation results (0 to 3° [load deg])by the second-axis between the different controllers and the Lead Compensator 55
5.19 Zoom in the load time response comparison of simulation results (0 to 3° [load deg]) by the first and second-axis between the different controllers and the Lead Compensator 56

6.1 Interference Forces in the Horizontal Two-Axes Robot Arm 58

6.2 Vibrations due to J2 Torque 1st Experiment. J1 moves to 3 degrees and J2 Servolocked . . . 59
6.3 J1 Response with J2 Interaction Semiclosed 1 DOF . . . 60
6.4 J1 Response with J2 Interaction Semiclosed 1 DOF . . . 61

7.1 Lead Compensator Simulink Model . . . 63
7.2 Simulation results (0 to 3° [load deg]) by the first-axis Lead Compensator control system . . . 64
7.3 Simulation results (0 to 3° [load deg]) by the second-axis Lead Compensator control system . . . 65
7.4 Lead Lag Compensator Simulink Model . . . 66
7.5 Lead Lag Compensator Bode Diagram . . . 67
7.6 Simulation results (0 to 3 [load deg]) by the second-axis Lead Lag Compensator control system . . . 68

A.1 Sine Sweep Frequency for an Adaptive Controller . . . 73

B.1 Semiclosed 1DOF. J1 moves to 3°, J2 moves to [0, +3, -3][°] respectively . . . 75
B.2 Semiclosed 1DOF. J2 moves to 3°, J1 moves to [0, +3, -3][°] respectively . . . 76
B.3 Fullclosed 1DOF. J1 moves to 3°, J2 moves to [0, +3, -3][°] respectively . . . 77
B.4 Fullclosed 1DOF. J2 moves to 3°, J1 moves to [0, +3, -3][°] respectively . . . 78
B.5 Semiclosed 2DOF. J1 moves to 3°, J2 moves to [0, +3, -3][°] respectively . . . 79
B.6 Semiclosed 2DOF. J2 moves to 3°, J1 moves to [0, +3, -3][°] respectively . . . 80
B.7 Fullclosed 2DOF. J1 moves to 3°, J2 moves to [0, +3, -3][°] respectively . . . 81
B.8 Fullclosed 2DOF. J2 moves to 3°, J1 moves to [0, +3, -3][°] respectively . . . 82

C.1 Flowchart to design a controller . . . 84

Chapter 1

Introduction

This chapter discusses the motivation and background of this Master Thesis, objectives and structure of this thesis.

1.1 Background of this research

As background information to this Master's Degree Project, it should be noted that the research period is funded by the Erasmus+KA107 program. This program aims to encourage student mobility between partner countries outside Europe. The chosen destination was Japan, an avant-garde country in the field of Mechatronics Engineering. This research is the result of the teamwork of people from different nationalities. Thanks to the many academic agreements that the UPV has, it was possible to stay at Nagoya Institute of Technology (NIT). Professor Makoto Iwasaki, Head of Department of Electrical and Mechanical Engineering at NIT, was the supervisor during this period of research. In his laboratory, the work dynamic consist in continue the research of other students. This provides improvements and new points of view. Currently, the industrial robots of these companies are used for various fields such as: multiple kinds of automating lines production and work sites involving danger, wide range of transportation, assembly of products, welding, painting etc. [Noda, 1990] [Yonemoto, 1976]. Tasks that ask a high performance. Therefore, in order to realise an improvement in work efficiency and productivity of the production line, higher speed and higher accuracy positioning control performance is indispensable. Thus, this department performs I+D+i tasks for several key companies in robot manufacturing, such as Denso Company, supplier of the material of the present investigation.

1.2 Purpose of this research

The final objective of this group research is to construct a damping control system for the industrial four-axis horizontal SCARA robot with high speed and high accuracy positioning response. But various factors interfere with each other in the 4-axis SCARA robot. Thus a precise characteristic analysis and an evaluation are really difficult.
Therefore, in this research, a horizontal two-axis robot is used instead. It simulates the first axis and the second axis of the SCARA robot. This way, it's easier to eliminate the resonance vibration inherent to the robot construction and the vibration due to the interference force between the axes and to study the non-linearities. These are the main objectives established for the realisation of the current thesis.
In order to achieve this main objective, the following intermediate objectives have been proposed:

O1. **Understanding the previous work of other students**. For this part, papers and theses from already graduated students in the department have been read.

O2. **New Mathematical Model Identification Methods.** For the design of a good controller, it is necessary to obtain a mathematical model about the behaviour of the robot system. Two new identification methods are presented to improve the previous models developed by the previous students.

O3. **High speed and high accuracy positioning.** The robotics industry is very demanding, so it requires a high speed and high positioning accuracy in the robot to

accomplish such requirements. To achieve this important task, it is necessary: to suppress the natural frequencies, to compensate the non-linearities of the system and to eliminate the interference force between axes. In this way, different typologies of control are developed.

1.3 Structure of this thesis

This report has been organised as follows:

- **Chapter 1: Introduction** The background and purposes of this research are described.
- **Chapter 2: Description of the EUT** The system configuration of the horizontal two-axis robot (Equipment Under Test, henceforth referred to as EUT), the control system, and the structure and operation principle of the Harmonic Drive Gear used for the joint part, the target control specifications are described.
- **Chapter 3: Mathematical Model** An identification in the frequency domain is performed and mathematical models of the controlled object are obtained. Then, a new identification methods are presented to construct a numerical simulator. Finally the different identification methods are compared and commented.
- **Chapter 4: Reference and Time Response** The reference profile is defined so that it excites the first mode of vibration. So the validity of the designed controls can be tested. Experiments that will be used in the rest of the chapters are defined.
- **Chapter 5 Suppression of inter-axis interference force by load state quantity feedback control** A load state quantity feedback compensator is designed in order to suppress control performance deterioration due to the influence of the inter-axis interference force generated at the time of multi-axis drive. Furthermore, its effectiveness is verified by simulator and actual machine experiment.
- **Chapter 6 Inter-axis Interference Force** This chapter explains the interaction force in the equipment under test. Experiments are carried out and conclusions are drawn.
- **Chapter 7 Disturbance Testing Simulation** Chapter 7 deals with the Lead-Lag Compensator with disturbances to check the behaviour in simulations and a solution implemented to improve the controller, the Lead Lag Compensator.
- **Chapter 8 Conclusions** Research result and future study subjects will be described.

Chapter 2

Description of the EUT

In this chapter, the system configuration of the horizontal two-axis robot (Equipment Under Test, henceforth referred to as EUT), the control system, and the structure and operation principle of the Harmonic Drive Gear used for the joint part, the target control specifications are described.

2.1 Equipment Under Test Configuration

In this section, the horizontal two-axis robot used in this research is described.

2.1.1 Simplified *SCARA* Robot (2 axes)

The Equipment Under Test is a robot with 2DOF (Degrees of Freedom). It comes from a simplification of a SCARA robot with 4DOF. The prismatic link and the rotational joint in the end effector, the place destined to the tool, where suppressed. As it is mentioned in section 1.2, various factors interfere with each other in the SCARA robot with 4DOF, so precise characteristic analysis and evaluation are more difficult. That is the reason why, in this research it is used a horizontal two-axis robot which simulates the first axis and the second axis of the SCARA robot. An encoder was set up for evaluating the behaviour of the load end and model joints. In this equipment under test, the Harmonic Drive Gear (henceforth referred to as HDG) was used as the speed reducer in the joint part. Fig.2.1 shows an overview of the EUT that reproduces the characteristics of the first axis and the second axis of the 4-axis SCARA robot. Fig.2.2 shows a schematic diagram of the EUT including the control system. The EUT has an arm load that simulates the weight for the suppressed parts. In addition to the two-axis robot, EUT consists in a controller that performs command generation and control calculation, a command generation device (*TP: Teaching Pendant*) (resolution: $8192 pulse/rev$) used for positioning experiments, and a PC for data storage. As shown in Figure 2.3, an encoder is installed at the end of the motor for motor position detection and control. A semi closed loop system for driving the load is constructed based on the motor position information. Forthermore, in order to measure and evaluate the behaviour of the load end via the HDG, an encoder for placement measurement is installed. In the case of full closed control, this load axis encoder is used as a control detector. To sum up, the EUT is conformed by two joints with 1 motor, 1 HDG and 2 encoders per joint. So the HDG behaviour and the non-linearities can be tested. Differentiating between motor (encoder prior HDG) and load (encoder after the HDG). The Fig. 2.4 shows a scheme with this differentiation.

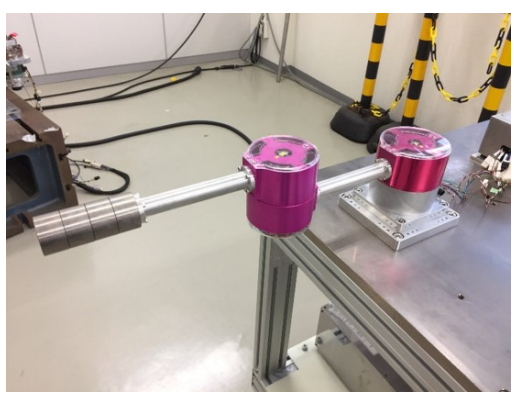

Figure 2.1: Equipment Under Test

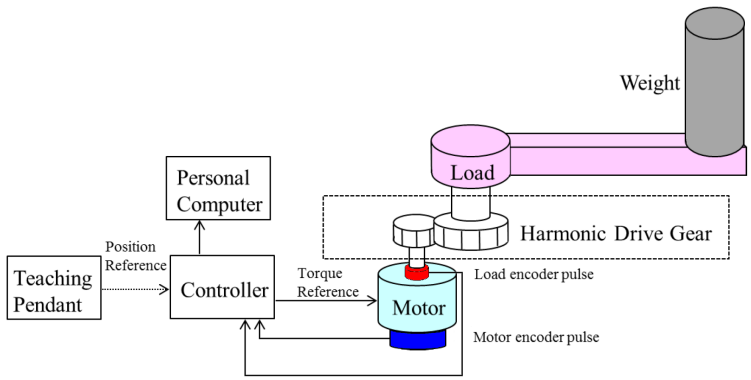

Figure 2.2: Schematic diagram of the EUT

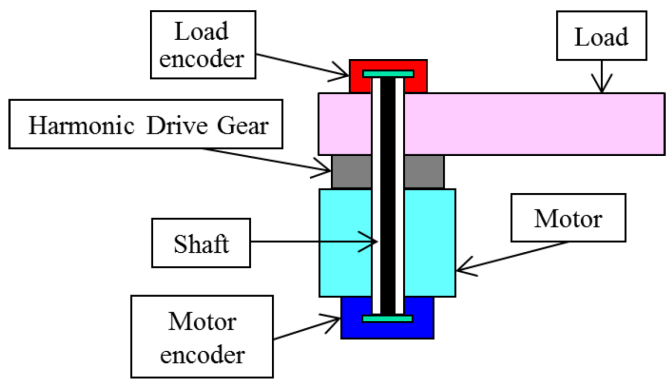

Figure 2.3: Schematic diagram of the Encoder

2.1.2 Joint actuator specifications

Table 2.1 and Table 2.2 show the specifications of the arm drive actuator, respectively.

2.1.3 P-PI DENSO Controller

As shown in the block diagram of Fig. 2.5, the motor semi-closed loop control system for this test device is constructed with a P (proportional) control system on the motor position and a PI (proportional integral) control system on the motor speed. In the figure, $P(s)$ is the controlled object, K_{pp} is the position proportional gain, K_{vp} is the speed proportional gain, K_{vi} is the speed integral gain, θ_m is the motor position, θ_l is the load position, $\tau_r ef$ is the torque command and r is the reference position. Each compensator gain is shown in Table 2.3. This controller is proportioned by Denso Corporation.

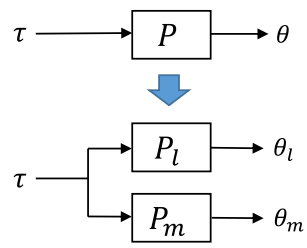

Figure 2.4: Scheme of Plant Model differentiation. Motor and Load

Table 2.1: First axis Drive Actuator (FHA-11C-100) Specifications

Rated torque	0.055 Nm
Instantaneous maximum torque	0.250 Nm
Torque limit capacity	0.1380 Nm
Maximum rotation speed	6000 rpm
Moment of inertia	6.7×10^{-3} kgm^2
Motor shaft encoder Resolution	131072 $pulse/rev$
Load axis encoder Resolution	1048576 $pulse/rev$
Gear ratio	100

2.2 *Harmonic Drive Gear*

2.2.1 HDG Characteristics. Structure and operation principle of the Harmonic Drive Gear

HDG is a reduction gear that elastically deforms a flexible cylindrical gear and utilises special meshing between gears [Cat, 2004] [Kazuto Imaichi, 2006]. Since a high reduction gear ratio is obtained in one stage and the number of parts is small this gear is, very thin, lightweight, large torque capacity and easy to incorporate. Furthermore, since there is essentially no backlash, it

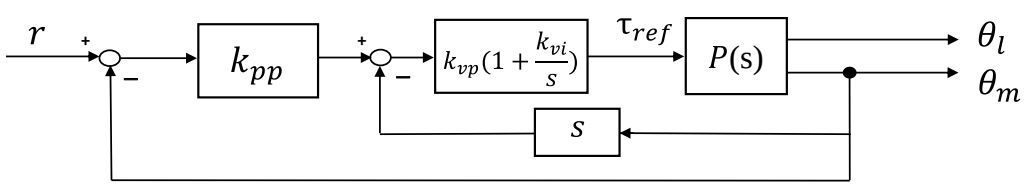

Figure 2.5: Actual machine control system block diagram

Table 2.2: Second axis Drive Actuator (FHA-8C-100) Specifications

Rated torque	0.026 Nm
Instantaneous maximum torque	0.090 Nm
Torque limit capacity	0.083 Nm
Maximum rotation speed	6000 rpm
Moment of inertia	2.9×10^{-3} kgm^2
Motor shaft encoder Resolution	131072 $pulse/rev$
Load axis encoder Resolution	1048576 $pulse/rev$
Gear ratio	100

Table 2.3: Control system gain

K_{pp}	K_{vp}	K_{vi}
$2\pi \times 2.2$ rad/s	$2\pi \times 256.323$ rad/s	$1/(10 \times 10^{-3})$ rad/s

is widely used for machine tools and industrial robots suitable for highly accurate positioning [Misawa, 1991] [Takizawa, 2006]. The basic structure of HDG is shown in Figure 2.6. On the outer periphery of the elliptical cam, a wave generator (hereinafter referred to as WG) fitted with a thin ball and bearing, a cup-shaped flex spline (hereinafter referred to as FS) with teeth engraved on the outer periphery, teeth engraved on the inner periphery is composed of three parts of a circular spline of a rigid ring shape (hereinafter referred to as CS). Normally, FS is designed to have two teeth fewer than CS, and by inserting an elliptical WG into FS, FS elastically deforms and engages with CS. In this state, when the input shaft WG is rotated, the meshing position is sequentially moved, and when the WG rotates once, FS moves in the reverse rotation direction by the difference of the number of teeth from CS. The transition of each component of HDG when rotating the WG is explained in Table 2.4. By taking out the operation of this FS as an output, the reduction ratio N can be expressed by the expression 2.1 by the number of teeth Z_{CS} of CS and the number of teeth Z_{FS} of FS.

$$N = \frac{F_{FS}}{Z_{CS} - Z_{FS}} \tag{2.1}$$

2.2.2 Nonlinear characteristics of wave gear

The results regarding non-linearities and their modelling which are in this section 2.2.2 and 2.2.3 have been provided by laboratory colleagues who are working on the same project.
This controlled system has various nonlinear characteristics. It is clear from many previous studies that HDG has its unique structure and nonlinear characteristics [Mizuno, 2008] [Oya, 2008]. Its main elements are listed below.

1. Nonlinear friction characteristic: Nonlinear Friction Characteristics Generated at Each Contact Portion of Reducer, Motor Shaft and Load Shaft.

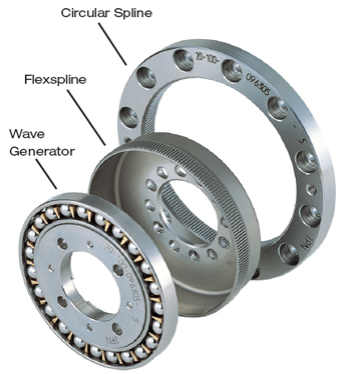

Figure 2.6: HDG Overview [Cat, 2004]

2. Nonlinear spring characteristics: Characteristic that the torsional rigidity changes nonlinearly due to the flexible structure of FS.

3. Angular transmission error: The angular transmission error defined above is classified into the following two according to, the cause of error occurrence.

   – Relative rotation synchronous component: An error component generated in synchronism with the relative rotation of each component of HDG due to machining error of the gear and axial misalignment between the reduction gear and the load.

   – Nonlinear elastically deformable component: Nonlinear error component including hysteresis characteristics other than the nonlinear spring characteristics among elastic deformation components caused by the flexible structure of FS.

2.2.3 Modelling Non-Linearities friction characteristics

In this subsection, general nonlinear friction characteristics of the mechanism including the HDG and model the static friction characteristics by constant speed test are analysed.

A. Outline of Nonlinear Friction Characteristics Friction static characteristics can be generally categorised as follows, and characteristics change depending on the driving speed region.

   1. Viscous Friction: dynamic friction proportional to speed
   2. Coulomb Friction: solid friction in operation state dependent on sign of speed
   3. Static Friction: friction applied at the start of operation from a stationary state

   Fig. 2.7 shows a conceptual diagram of friction characteristics when the speed is plotted on the abscissa and the frictional force is on the ordinate. Here, F_f is the frictional force, T_c is the Coulomb frictional force, D is the viscous friction coefficient, ω_s is the *Stribeck* velocity, and ω_m is the motor shaft speed. The figure shows that the

Table 2.4: Transition during driving of HDG

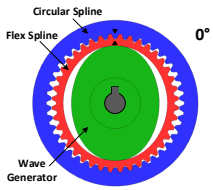	FS is deflected elliptically by WG and meshes with CS
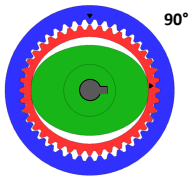	When WG is rotated in the clockwise direction, FS elastically deforms and the position of engagement moves sequentially
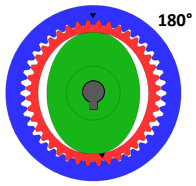	When WG rotates 180 degrees, FS moves counterclockwise by the number of teeth
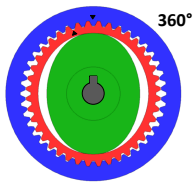	When WG rotates 360 degrees, FS moves counterclockwise by two teeth. It extracts this motion as output

maximum static friction acts at the time of starting and then transits to the region where the viscous friction dominates through the *Stribeck* effect showing the negative slope characteristic.

B. Modelling static friction characteristics by constant velocity test.

In this section, static friction characteristics are identified by a constant speed test. The constant speed test is a method of driving the motor at a constant speed and measuring friction characteristics from control input at constant speed driving.

Since the acceleration becomes 0 at constant speed driving, the influence of inertial force can be ignored, and the control input corresponds to friction. Therefore, static friction characteristics can be obtained by changing speed.

Constant speed test measurement results are shown in Fig. 2.8 and 2.9. As these figures show, the *Stribeck* effect is not confirmed in the actual machine friction characteristics, and *Coulomb* friction and viscous friction are dominant. Therefore, parameters of

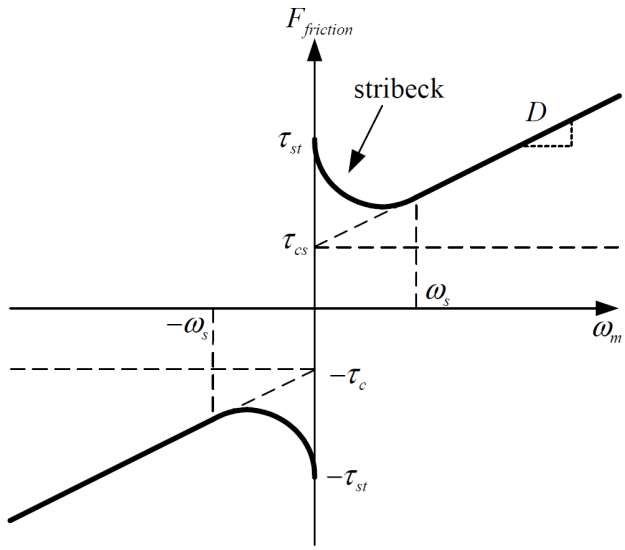

Figure 2.7: Concept of friction characteristics

viscous friction and *Coulomb* friction are identified by a first order polynomial approximation that uses least squares method based on measurement result of constant speed test. If the slope of the approximate polynomial is the viscous friction coefficient D and the offset is *Coulomb* friction τ_{CS}, the frictional force can be expressed by the equation 2.2 using the motor shaft speed ω_m.

$$Friction = \tau_c + D \cdot \omega_m \tag{2.2}$$

Parameters of the friction model identified and set are shown in Table 2.5 and Table 2.6. Here, the least squares method was applied to the measurement results in the low speed region (0 to 200 rpm), considering the velocity region near the settling. Figures 2.8 and 2.9 show actual friction characteristics in the speed region used in the evaluation command as black dots and friction models as blue lines.

Table 2.5: Result of friction parameter identification on the first axis

Coulomb Friction Force τ_{cl} (CW) $[Nm]$	1.829×10^{-2}
Viscous Friction Coefficient D_1 (CW) $[Nm/rpm]$	1.905×10^{-5}
Coulomb Friction Force τ_{cl} (CWW) $[Nm]$	1.782×10^{-2}
Viscous Friction Coefficient D_1 (CWW) $[Nm/rpm]$	1.639×10^{-5}

Table 2.6: Result of friction parameter identification on the second axis

Coulomb Friction Force τ_{cl} (CW) $[Nm]$	1.460×10^{-2}
Viscous Friction Coefficient D_1 (CW) $[Nm/rpm]$	1.493×10^{-5}
Coulomb Friction Force τ_{cl} (CWW) $[Nm]$	1.571×10^{-2}
Viscous Friction Coefficient D_1 (CWW) $[Nm/rpm]$	1.781×10^{-5}

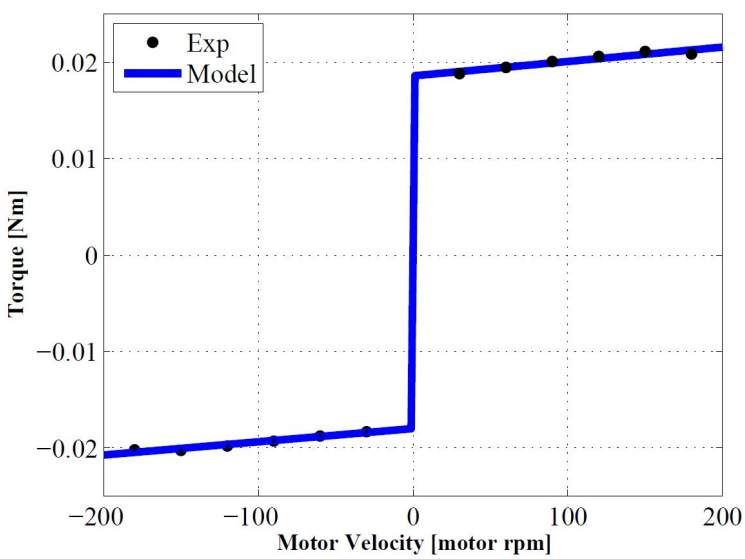

Figure 2.8: Results of modelling friction characteristics on first axis

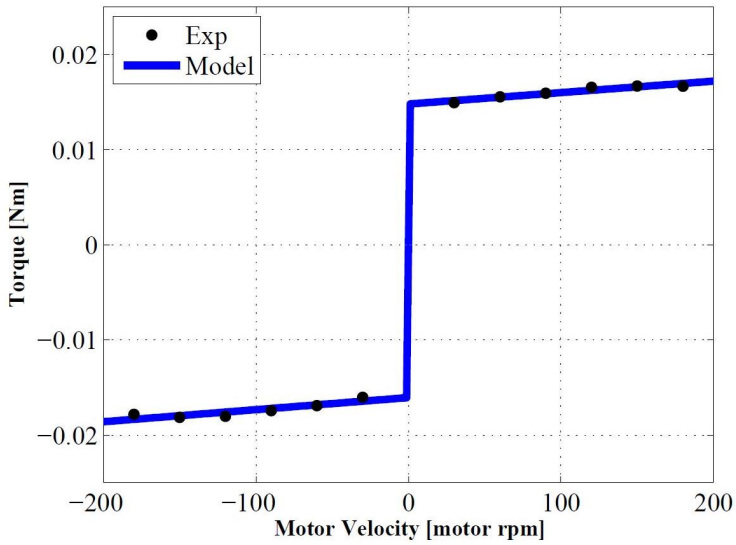

Figure 2.9: Results of modelling friction characteristics on second axis

Chapter 3

Mathematical Model

In this chapter, an identification in the frequency domain is performed and mathematical models of the controlled object are obtained. New identification methods are presented to construct a numerical simulator. The different identification methods are compared and commented.

3.1 Introduction

This chapter explains the identification process of the system in the frequency domain. A frequency sine sweep is performed in both joints (joint 1 and joint 2), to obtain a mathematical model that represents the behaviour of the system. The model called *previous mathematical model*, because it is the one used by the laboratory colleagues. Two new identification methods were proposed because they provide a more precise model from the frequency sine sweep experiment results. The two different identification methods are compared with the previous one used in the laboratory. The time response of both is tested and after that some conclusions are commented.

3.2 Sine Sweep

3.2.1 Experiments Characteristics

The frequency response analysis of the controlled object is carried out by performing a vibration test by a sinusoidal sweep method. Sinusoidal sweep is a method of applying a sinusoidal signal to a controlled object and obtaining frequency characteristics from the input/output response at that time. As a method of sinusoidal sweep, as shown in Fig. 3.1(a), there are a exciting method by constructing a closed loop system and a exciting method directly with a sinusoidal waveform without constructing a closed loop system as shown in Fig. 3.1(b). There is a way to do it [Nagamatsu, 1993]. In the former case, although the motor position/load position does not drift due to the closed loop system, it is experienced that the response waveform is distorted. On the other hand, since the latter does not constitute a closed loop system, it is possible to excite the controlled object with an arbitrary signal, but drift may occur. Since there is restriction on the movable range in this system, a sinusoidal sweep is performed on the closed loop system shown in Fig. 3.1(a) under the experimental conditions in Table 3.1 and the frequency characteristics are measured. The sine sweep frequency experiments input signal was the torque, and the amplitude used was the nominal torque. A load weight (1000 kg) was placed in the end effector. Firstly, a sine sweep in the first joint while the second joint servo-locked was carried out. Secondly, a sine sweep in the second joint while the first joint servo-locked was done. Fig. 3.2 shows the frequency characteristics of the first axis of the actual horizontal two-axis scalar robot, and Fig. 3.3 shows the frequency characteristic of the second axis. Both of these frequency characteristics were measured under the conditions shown in Table 3.1. In the figure, the blue line is from the torque input to the motor position, and the red line is the frequency characteristic from the torque input to the load position. Figures 3.2 and 3.3, motor and load are in the vicinity of 10 Hz for both the first axis and the second axis.

Table 3.1: Sine sweep measurement condition

Measurement frequency range $[Hz]$	1-1000
Number of measurement points	1000

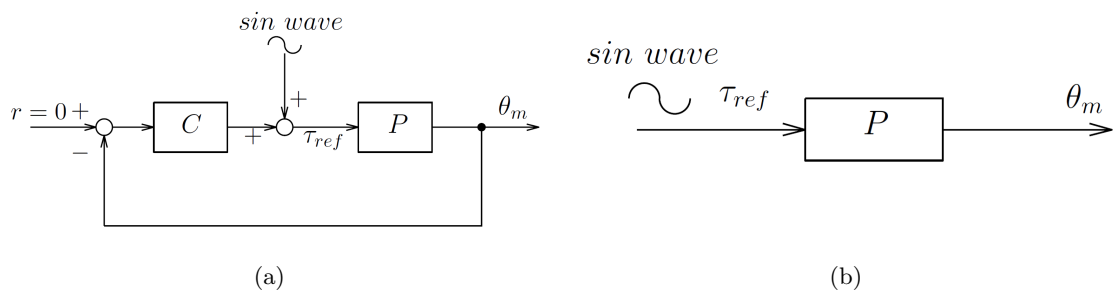

Figure 3.1: Control system block diagram at frequency characteristic measurement

3.2.2 Experiment Results

Figures 3.2 and 3.3 show the frequency sine sweep for the first joint and the second joint respectively. The blue line shows the torque corresponding to the motor, prior to the HDG, the motor; and the red line to the frequency sine sweep after the HDG, the load.

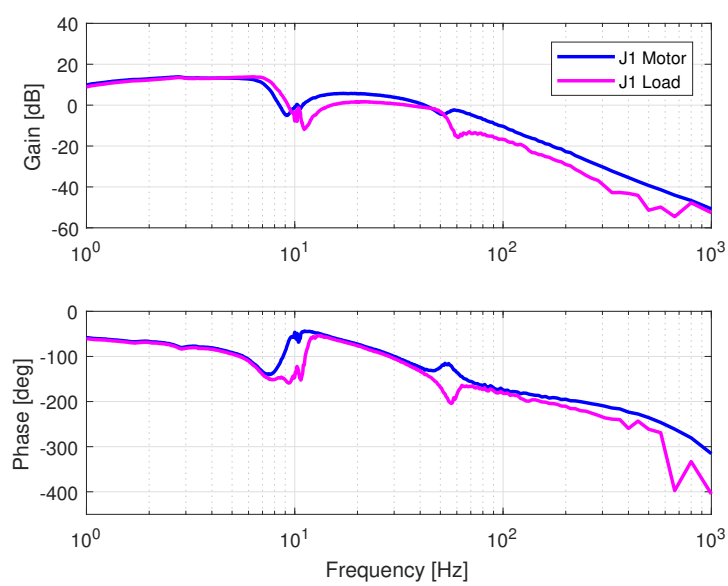

Figure 3.2: Frequency characteristics of the first axis of a bi-axial $SCARA$ robot

Difference in the frequency characteristics from the load and the motor can be appreciated. This is due to the HDG and the non-linearities. There is a primary vibration mode that is in phase, and a secondary vibration mode in which the motor and the arm are in opposite phases near 50 Hz. The factors will be examined and the controlled object will be modelled by the mathematical model and the numerical simulator in next section 3.3. The tertiary

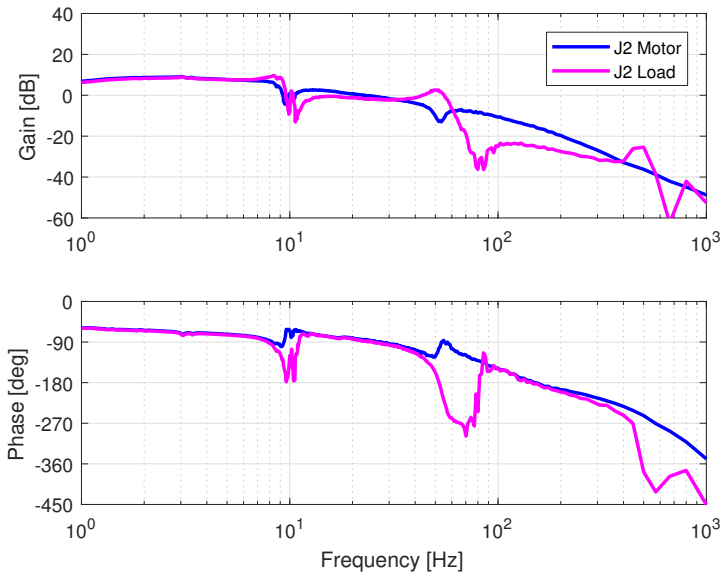

Figure 3.3: Frequency characteristics of the second axis of a bi-axial $SCARA$ robot

vibration mode exists only on the load side of each axis, but it can be ignored as it will be explained in the section 3.3.2. Thus it will be modelled up until the secondary vibration mode.

3.3 Previous Mathematical Model

3.3.1 Construction of Numerical Simulator

As shown in section 3.2.2, the frequency characteristics of the two axes of the controlled object each have two vibration modes. From Fig. 3.2 and 3.3, the primary vibration mode of each axis is in phase, but it is difficult to reproduce with the 2 inertial system physical model. Therefore, in this study, the controlled object is modelled by the mathematical model and the numerical simulator.

3.3.2 Building a mathematical model

As described in the previous section, in this study, it is modelled the controlled object by mathematical model. The tertiary vibration mode exists only on the load side of each axis due to the configuration of the encoder, but the vicinity of 450 Hz where the vibration mode exists is out of the control band and the influence on the response waveform is small and can be ignored. Thus, as it is said, in this research, we model up to secondary vibration mode. The procedure for constructing the mathematical model is shown below. The modelling up

to the secondary vibration mode is expressed by the following equation (3.1) using the rigid body mode, the second order delay system, and the delay time.

$$P(s) = (\frac{k_0}{s^2} + \sum_{i=1}^{2} \frac{k_i}{s^2 + \xi_i \omega_i s + \omega_i^2})e^{-Ls} \tag{3.1}$$

k_0, k_i, ξ_i, ω_i and L are the rigid body mode coefficient, the number of mode systems of the ith vibration mode, the attenuation coefficient, the resonance angular frequency and the delay time, respectively. Based on the experimental results, each parameter was determined by trial and error so that the error of the position response in the transient response was small. Table 3.2, Table 3.3, Table 3.4, Table 3.5 list each parameter. Fig. 3.4, Fig. 3.5, Fig. 3.6, and Fig. 3.7 show the results of modelling the controlled object by mathematical equation.

Table 3.2: First axis motor side plant frequency characteristics

	i	$k_{mi}[mm/Ns^2]$	ξ_{mi}	$\omega_{mi}[rad/s]$
Rigid body mode	0	16500	-	-
Primary vibration mode	1	69000	0.09	$2\pi \times 21$
Secondary vibration mode	2	25000	0.09	$2\pi \times 58$
Dead time $L_m[s]$	0.00044			

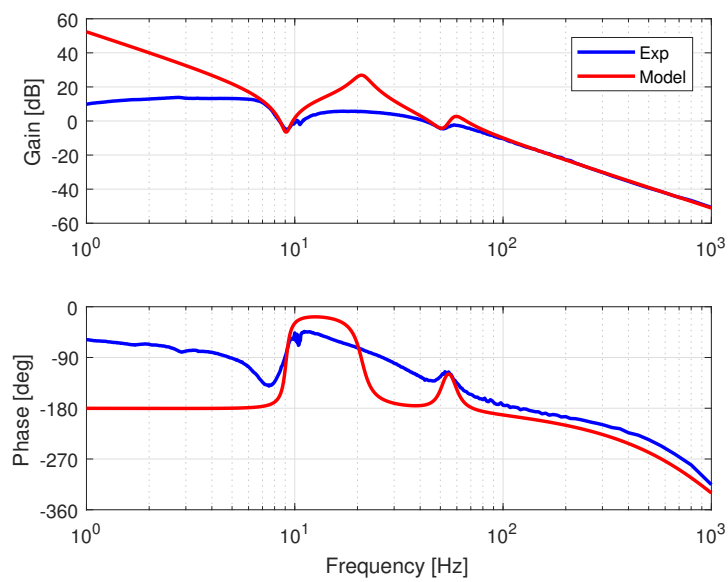

Figure 3.4: Frequency characteristic model from the torque command to the motor position on the first axis

Table 3.3: First axis load side plant frequency characteristics

	i	$k_{mi}[mm/Ns^2]$	ξ_{mi}	$\omega_{mi}[rad/s]$
Rigid body mode	0	16500	-	-
Primary vibration mode	1	50000	0.25	$2\pi \times 21$
Secondary vibration mode	2	-13000	0.11	$2\pi \times 53$
Dead time $L_m[s]$	0.00044			

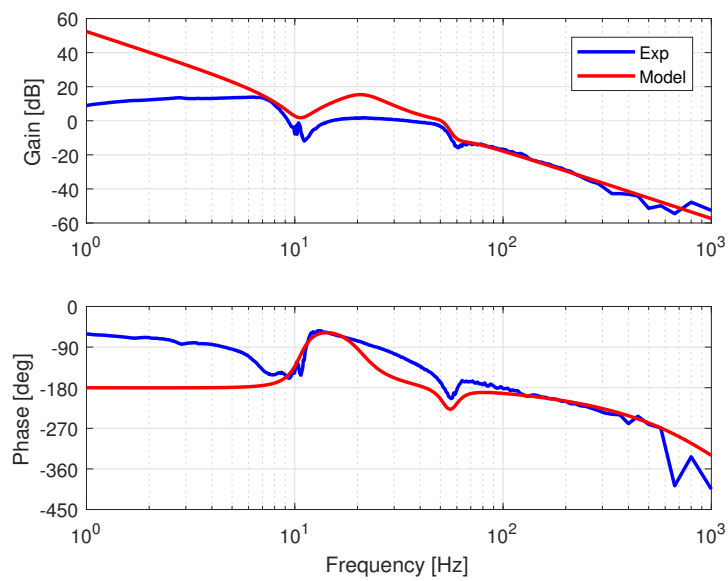

Figure 3.5: Frequency characteristic model from the torque command to the load position on the first axis

3.4 New Identified Mathematical Model

3.4.1 Preamble

In this section, two new identification methods are proposed with the target to get a better mathematical model which allows to design a better controller. The first one is a *Matlab* function tool called *Ident tool*, where it can be obtained a mathematical models of dynamic systems from measured input-output data. The second one is a fitting identification method, it works as *Ident tool* does it, but it works in a manual way.

3.4.2 Matlab Ident Tool

This tool is a function from *Matlab* which allows constructing mathematical models of dynamic systems from measured input-output data. It lets to create and use models of dynamic systems not easily modelled from first principles or specifications. *Ident tool* allows to estab-

Table 3.4: Second axis motor side plant frequency characteristics

	i	$k_{mi}[mm/Ns^2]$	ξ_{mi}	$\omega_{mi}[rad/s]$
Rigid body mode	0	35000	-	-
Primary vibration mode	1	35000	0.13	$2\pi \times 13$
Secondary vibration mode	2	30000	0.08	$2\pi \times 65$
Dead time $L_m[s]$	0.00055			

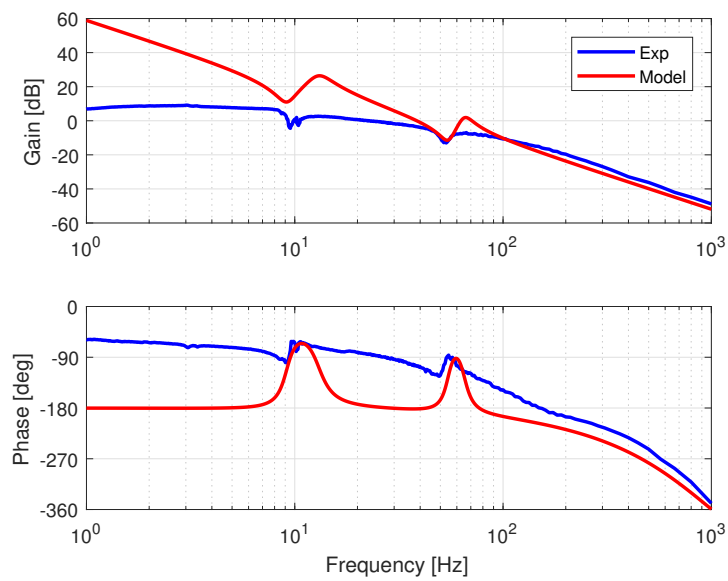

Figure 3.6: Frequency characteristic model from the torque command to the motor position on the second axis

lish the number of poles and zeros in the mathematical model. So it was tried with different types of combination to obtain the nearest frequency response in comparison with the sine sweep frequency experiment.
Fig. 3.8 shows in grey colour the frequency sine sweep experiment, and in red colour the mathematical model obtained with *Ident tool*. Fig. 3.8(a) shows a mathematical model with 2 poles and 3 zeros, where it can not be observed the second natural frequency peak. The same mode, in Fig. 3.8(b), it can be observed a mathematical model with 8 poles and 7 zeros, and it can not be observed the second natural frequency peak due the the second vibration mode. In Fig. 3.8(c), a mathematical model with 30 poles and 29 zeros is obtained, being the most precised model achieved with a $97,55\%$ of similitude.

Table 3.5: Second axis load side plant frequency characteristics

	i	$k_{mi}[mm/Ns^2]$	ξ_{mi}	$\omega_{mi}[rad/s]$
Rigid body mode	0	35000	-	-
Primary vibration mode	1	38000	0.14	$2\pi \times 15$
Secondary vibration mode	2	-40000	0.07	$2\pi \times 54$
Dead time $L_m[s]$	0.00079			

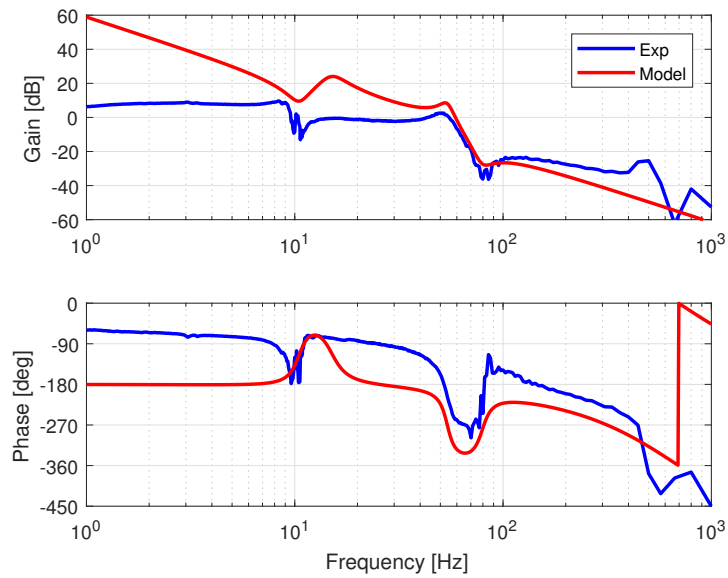

Figure 3.7: Frequency characteristic model from the torque command to the load position on the second axis

3.4.3 Fitting Identification

Fitting Identification works similar to *Matlab Ident tool*, but in this case, the parameters can be modified in order to improve the mathematical model manually through code in *Matlab*. This allows to use less poles and zeros to get a high similitude. The procedure of how to make the fitting is shown below:

- 1st**: Fitting Global Actuator Behaviour**
- 2nd**: Fitting First Resonance Peak**
- 3rd**: Fitting Second Resonance Peak**
- 4th**: Fitting Behaviour at Low Frequencies**

The Fitting Identification shown below, it is referred to the motor in the first joint. In the first fitting, the global actuator behaviour is adjusted to a fourth order transfer function

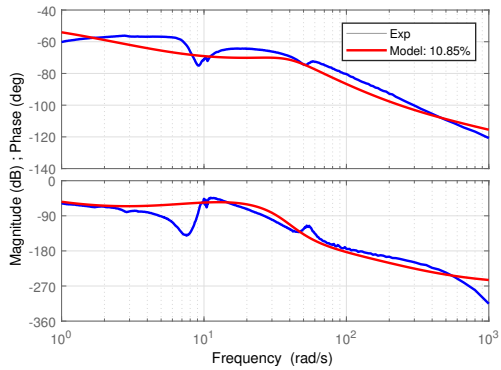

(a) Math. Model with 3 poles and 2 zeros. Similitude: 10.85%

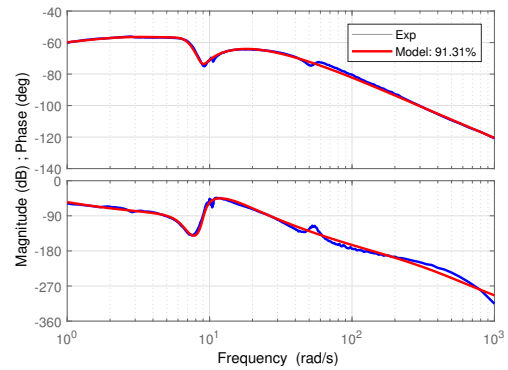

(b) Math. Model with 8 poles and 7 zeros. Similitude: 91.31%

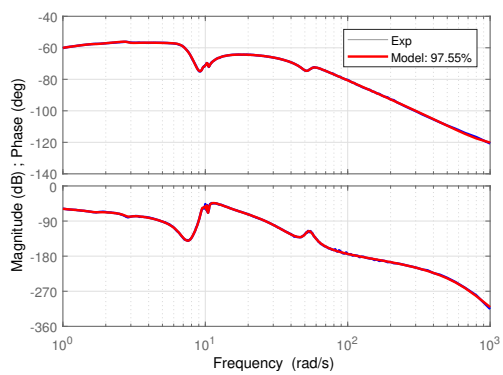

(c) Math. Model with 30 poles and 29 zeros. Similitude: 97.55%

Figure 3.8: Identified Mathematical Model with Ident Tool Function

($G_1(s)$). The number of poles and zeros used is chosen based on trial and error, being proved that it is the model that best represents the behaviour of the actuator. Fig. 3.9 shows in blue line the frequency sine sweep experiment and in red line the transfer function obtained with 3 zeros and 4 poles.

In the second and third fitting, the first and the second resonance peak are independently adjusted respectively. Both are a second order transfer function ($G_2(s)$ & $G_3(s)$). Gain and phase have to be zero. Equation 3.2 shows the transfer function represented by the system in the 2nd and 3rd fitting. The peak is adjusted by only modifying through trial and error the values of a, b, c and d, so a peak with same frequency can be obtained.

$$G_{2,3}(s) = \frac{s^2 + as + b}{s^2 + cs + d} \tag{3.2}$$

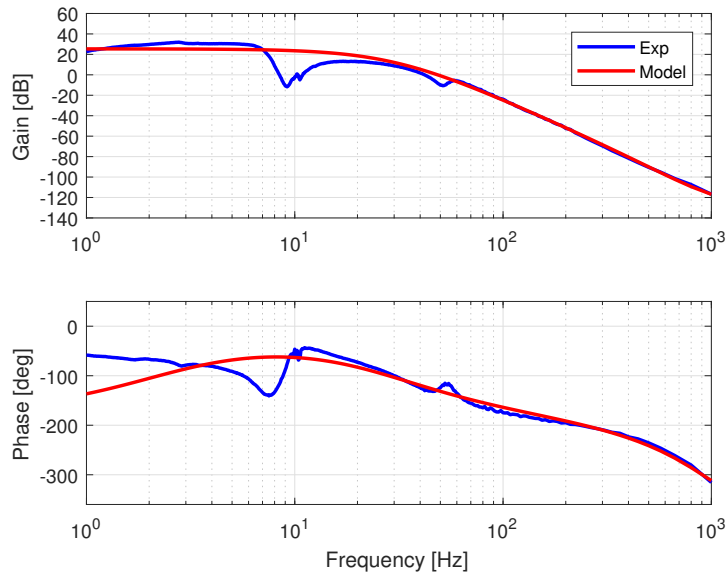

Figure 3.9: First Fitting: Global Actuator Behaviour $G_1(s)$

The Fig. 3.10 shows the fitting in the first and second resonance peak.
A final transfer function can be obtained as multiplication of modules and addition of phases. $G(s) = G_1(s)G_2(s)G_3(s)$. The Fig. 3.11 shows the fitting result, where the amplitude of the peak has been adjusted until matching size and frequency axis position with the frequency sine sweep experiment values. At low frequencies can be observed that the mathematical model $G(s)$ is not very precise, so it can be improved with a fitting behaviour at low frequencies. Fig. 3.12 shows the transfer function bode diagram in the fitting behaviour at low frequencies ($G_{lf}(s)$).
The new fitting result improved is the result of multiplication of modules and addition of phases with the prior model (G(s)) as: $G^*(s) = G_{lf}(s)G(s)$. The Fig. 3.13 shows the fitting result improved. The green line shows the previous transfer function $G(s)$, and the red line shows the improved transfer function with better behaviour at low frequencies ($G^*(s)$).
The fitting identification method was used, both in motor and the load, in the first and second joint. Fig. 3.14 shows the fitting result for motor and load, in the first and the second joint.

3.5 Mathematical Models Comparison

In order to compare the new identification method (fitting identification), the previous mathematical models and the new identified mathematical models are graphed in the same figure. Fig. 3.15 shows the motor and load, in the first and second joint. The blue line is the frequency sine sweep experiment, the red line is the previous mathematical model, and the green line is the new fitting identification method.

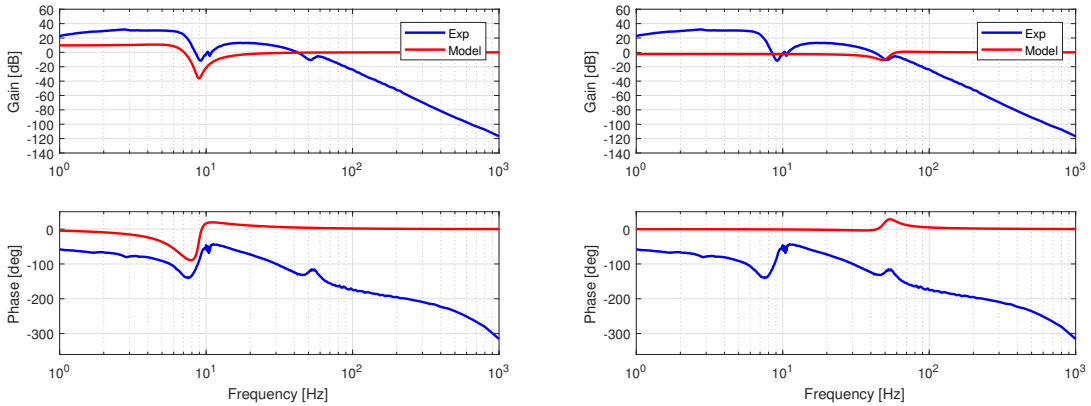

(a) Adjustment of 1st Resonance Peak $G_2(s)$ (b) Adjustment of 2nd Resonance Peak $G_3(s)$

Figure 3.10: Second and Third Fitting

3.6 Mathematical Models Conclusions

After performing the system identifications in different ways, and comparing both, it should be noted that a more accurate mathematical model is accomplished. The new identification method yields better results in terms of similarity with the frequency sine sweep experiment. A priori, it could be said that having made a better identification in the system's plant, the results obtained in the simulations would have greater affinity with those that contributed the experiments. After testing the time response of both the previous mathematical model (red line in Fig 3.15) and the new identified mathematical model (green line in Fig 3.15), it can be affirmed, on the one hand, that the new identified mathematical model is more accurate than the previous mathematical model. But as a counterpart, the new identified mathematical model is unstable in the time response, not as the previous mathematical model, which has a stable time response. Table 3.6 summarises the above.

Table 3.6: Summarise of Math. Model Conclusions

	Previous Mathematical Model	New Identified Math. Model
Frequency Domain	Imprecise	Precise
Time Domain	Stable	Unstable

During the six months research period, the mathematical model identification was carried out according to the new proposal (fitting identification) explained in section 3.4.3. After the end of the research period, the laboratory colleagues published a paper demonstrating that the methodology used in the sine sweep experiment was incorrect. In this paper [Sugiura et al., 2017], a study on Frequency Response Analysis (FRA) using friction model for frictional systems was carried out. The frequency response of the plant as in this research was analysed, where a plant system shows different frequency characteristics depending on the

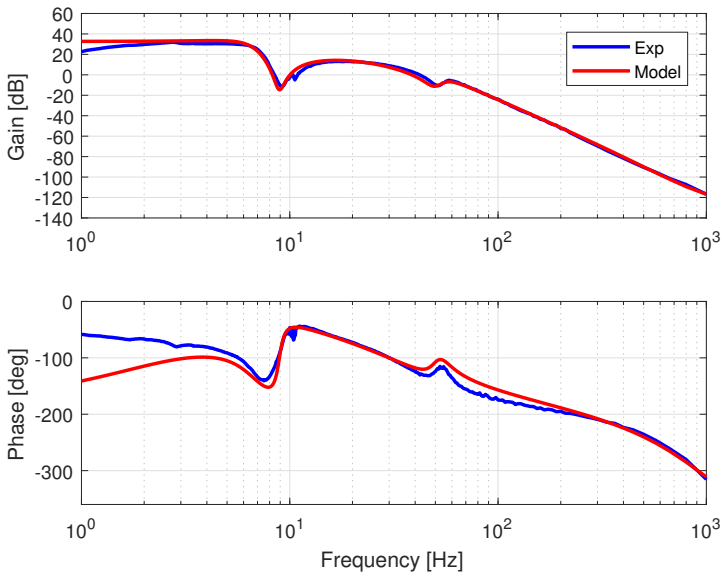

Figure 3.11: Fitting result $G(s)$

excitation amplitude. This variation of the superficial plant characteristic is caused by non-linear properties. Therefore, the conventional method cannot express the actual linear plant characteristics. Thus, the proposed FRA from the laboratory colleagues with different excitation conditions can precisely estimate the actual linear plant characteristics. Hence, it tests why the time response in the new identification method was unstable. Once again, as future tasks, the development of this identification method (fitting identification), with the target to obtain a better identification can be continued as in the chapter 8 will be commented.

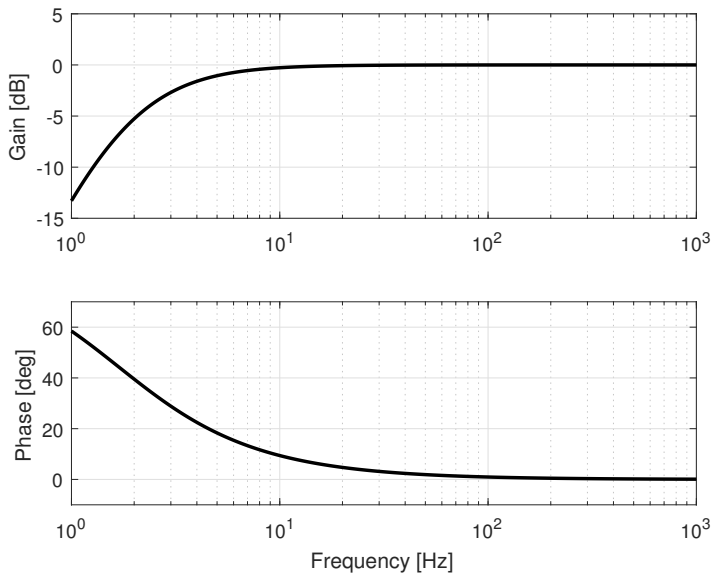

Figure 3.12: Transfer function bode diagram in the fitting behaviour at low frequencies $G_{lf}(s)$

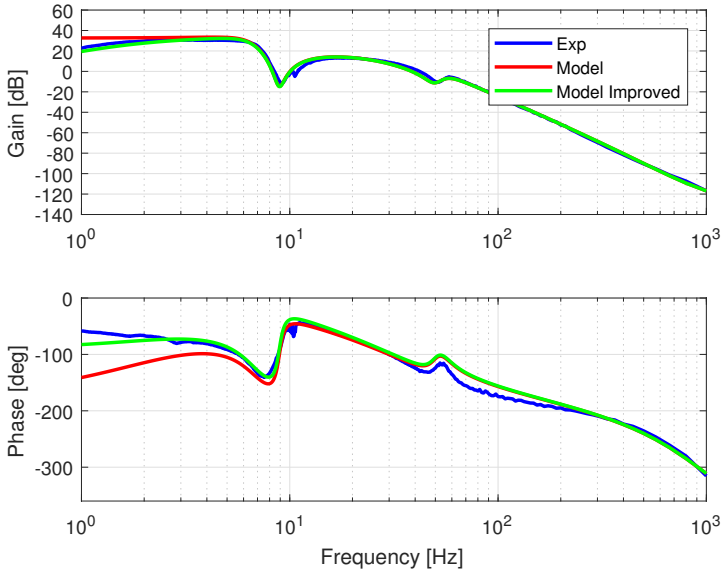

Figure 3.13: Fitting Result Improved $G^*(s)$

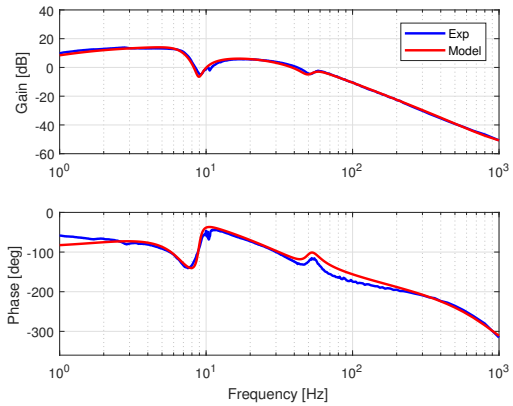

(a) J1 Motor Mathematical Model

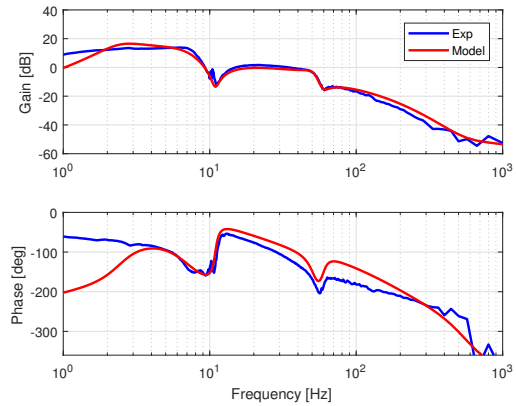

(b) J1 Load Mathematical Model

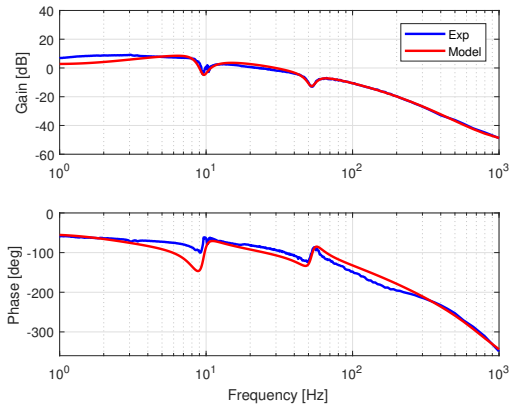

(c) J2 Motor Mathematical Model

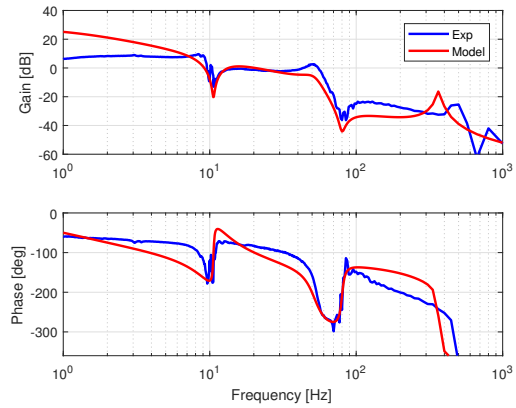

(d) J2 Load Mathematical Model

Figure 3.14: Joint 1 & 2, motor and load fitting identification

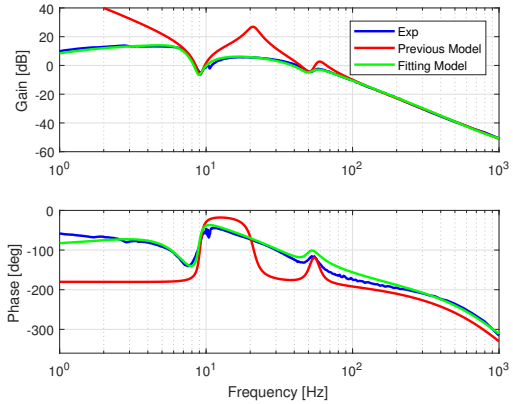

(a) J1 Motor Mathematical Model

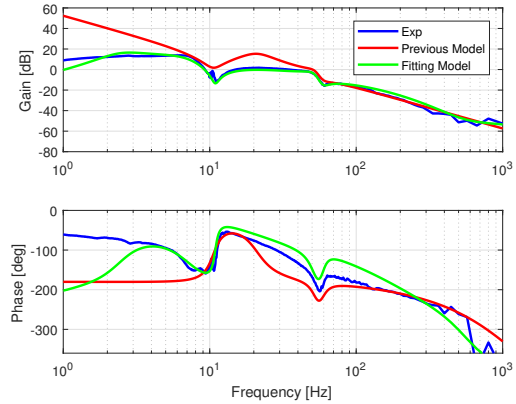

(b) J1 Load Mathematical Model

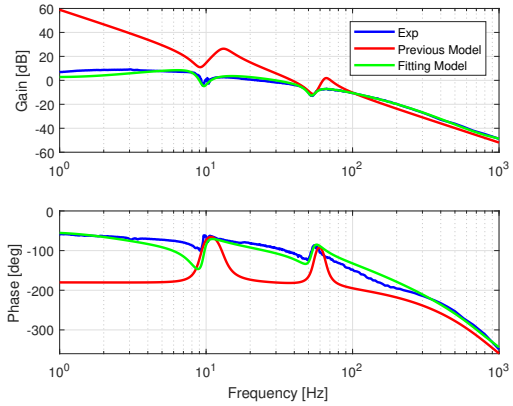

(c) J2 Motor Mathematical Model

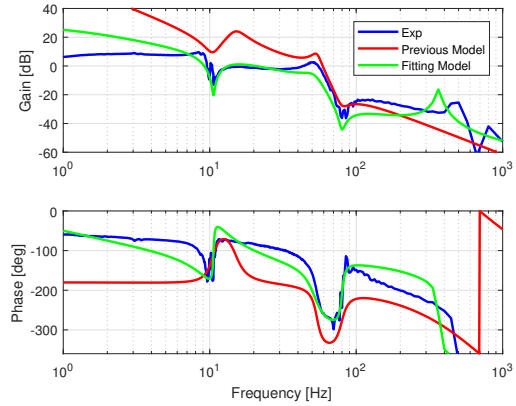

(d) J2 Load Mathematical Model

Figure 3.15: Comparison between previous and new identified mathematical model

Chapter 4

Reference and Time Response

This chapter defines the reference profile so that it excites the first mode of vibration so that test the validity of the designed controls can be tested. Experiments that will be used in the rest of the chapters are defined.

4.1 Introduction

This chapter describes the characteristics of the reference that will be used to test the behaviour of the controllers developed in chapter 5. In the previous chapter, two natural frequency peaks, located in a determined frequency ranges, around 10 and 60 Hz (see section 3.2.2 were obtained by frequency sine sweep. As will be shown in chapter 5, it is desired to suppress vibrations due to the first natural frequency peak, (around 10 Hz), by using a dynamic inversion control, ie a control with feed-forward loop. Thus, the reference should excite the first natural frequency peak. So different experiments of positioning were carried out to check which angle excited this frequency peak.

4.2 Reference Characteristics

In the EUT, the control signal input of the plant is the torque, which is directly proportional to the acceleration. Therefore the reference must not exceed the torque limits capacity of the motor and must be continuous in time because a continuous signal must always have a finite value and must be integrable. For this, a second order polynomial reference is chosen as the wave profile with s-shape. Due to the fact that acceleration is proportional to the torque, and it has a square wave profile, if a first derivative from the acceleration signal is obtained, a trapezoidal motion profile will be achieved, the velocity. With a second derivative from the acceleration signal, the s-shape wave profile will be obtained, the position. Analysing the s-shape wave, with different positioning experiments, rise time and settling time can be measured, thus obtaining the frequency. For the EUT, T corresponds with a semi-period, so a complete period corresponds to $2T$, and the relation between period and frequency, is shown in equation 4.1.

$$F = \frac{1}{2T} \tag{4.1}$$

In section 3.3.2, it was found for both joints that the first fundamental frequency peak for $J1$ was at a frequency of 9.17 Hz and for $J2$ at a frequency of 9.52 Hz. Therefore, it is necessary to find a $2T$ that is close to this natural frequency. Fig. 4.1 shows the reference path obtained by derivating twice the acceleration signal. Thus obtaining a s-shape reference, which will be used in the different positioning experiments.

4.3 Angle Reference Test

In order to obtain the angle reference, different positioning experiments were carried out. The Table 4.1 shows the period and the frequency for every experiment depending of the reference positioning.
In view of the results, the reference angle that most seems to excite the first natural frequency peak is the angle of 3 degrees, with 9.35 Hz. Fig. 4.2 shows the acceleration, velocity and position references at 3 degrees, where the frequency through the period can be obtained.

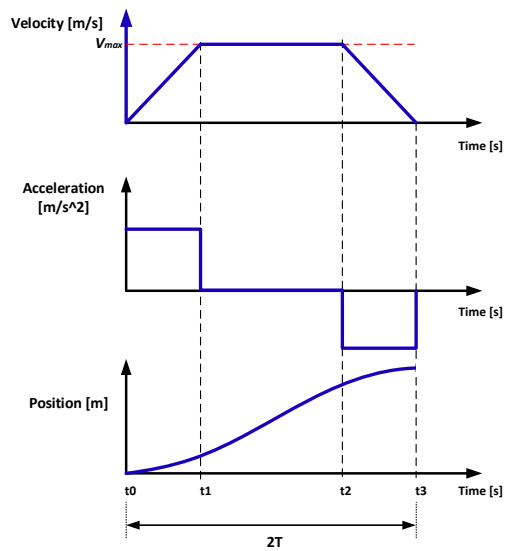

Figure 4.1: Reference waveform, Acceleration, Velocity and Position

Table 4.1: Angles test results

Degree $[deg]$	1	2	3	4	5	10	15	30	45
Period (2T) $[s]$	0.07	0.087	0.107	0.115	0.127	0.177	0.2	0.283	0.37
Frequency $[Hz]$	14.29	11.49	9.35	8.70	7.87	5.65	5.00	3.53	2.70

4.4 Time Response Angle Reference. Verification of actual machine response reproducibility by simulator

Three graphs appear in the motor and load position response figures. The graph on the left is used to show the delay time between the reference and the system because of friction. While the upper right graph shows the behaviour around the settling area. In both graphs the motor position is converted into load angles, dividing the motor angle by the coefficient of reduction. Finally, the lower graph shows the trajectory response error between the actual response and the simulation response. This verifies the real-machine response reproducibility of the constructed model

A numerical simulator using the mathematical model constructed in the section 3.3 is constructed and verify the validity of the model by comparing it with the positioning response of the real machine. For the control system at positioning response, the semi-closed control system shown in Figure 2.5 in the section 2.1.3 is used. Fig. 4.3, Fig. 4.4, Fig. 4.5 show the first axis motor position response, load position response, motor torque command, Fig. 4.6, Fig. 4.7 and Fig. 4.8 show the second axis motor position response, load position response,

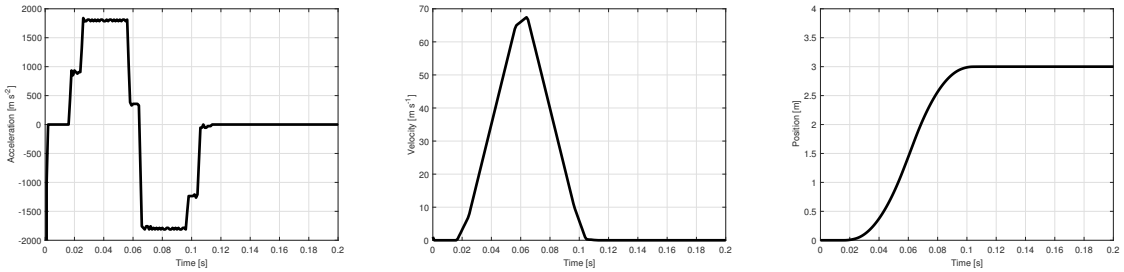

(a) Acceleration Reference (b) Velocity Reference (c) Position Reference

Figure 4.2: Acceleration, Velocity and Position Reference to 3 Degrees

motor torque command respectively. Three graphs appear in the motor and load position response figures. The graph on the left is used to show the delay time between the reference and the system because of friction. While the upper right graph shows the behaviour around the settling area. In both graphs the motor position is converted into load angles, dividing the motor angle by the coefficient of reduction. Finally, the lower graph shows the trajectory response error between the real machine response and the simulation response. This verifies the real-machine response reproducibility of the constructed model. In the figures, the black line is the position command, the blue line is the real machine response, the red line is the simulator response, the horizontal black dot lines in the position response diagram is the target settling time ± 0.0193 [load deg] (described in the future section 5.1.1), the vertical black dot line is the target settling time after the position command reach in 0.1 seconds (described in the future section 5.1.1), the horizontal black dotted line in the torque command diagram shows the torque limit capacity. From Fig. 4.3, Fig. 4.4, Fig. 4.6, and Fig. 4.7, the overshoot amount and attenuation in transient response are reproduced well for both motor position and load position on each axis. On the other hand, there is a delay in the response of the real machine in the rising time. From Fig. 4.5 and Fig. 4.8, noise is seen in the settled torque, but these occur due to the influence of quantization noise. Continuous speed reversal around $\omega_m = 0$, the *Coulomb* frictional force sharply changes to positive and negative. This is due to the phenomenon of switching. In order to eliminate this, using Coulomb friction in the friction model expressed by equation 2.2 instead of τ_c, using $\tau_c \cdot \tanh(B\omega_m)$ with the gradient B in $\omega_m = 0$. It is necessary to connect smoothly in the vicinity, but when doing it, since the reproducibility of the torque in the transient response is greatly deteriorated, it will dare to leave noise. From the above results, it was possible to construct a simulator that evaluates the performance of actual machine response.

4.5 Experiments Determination

In order to test the controllers that have been developed in the chapter 5, five different experiments are defined, where $J1$ and $J2$ are moved to the excitation position of the first natural frequency peak, 3 degrees, with different conditions. In the experiment 1, $J1$ moves

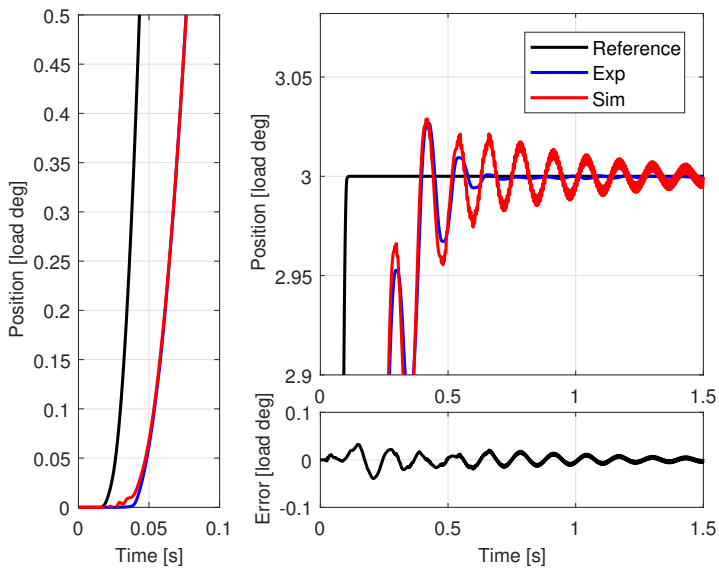

Figure 4.3: First axis motor position response reproducibility

to +3 degrees and $J2$ is servo-locked. In the experiment 2, $J2$ moves to +3 degrees and $J1$ is servo-locked. In this way, the behaviour of every joint independently can be tested without interaction force between them. In order to test the interaction force (described in the future chapter 6) when both are moving, experiment 3, 4 and 5 were defined. In the experiment 3, both joints move to +3 degrees. In the experiment 4, $J1$ moves to +3 degrees and $J2$ moves to −3 degrees, and in the experiment 5, $J1$ moves to −3 degrees and $J2$ moves to +3 degrees. Experiments 4 and 5, joint 1 and joint 2 move both in opposite direction, to check all possible combinations. The experiments are listed below:

- Experiment 1: $J1$ [3°] & $J2$ [0°]. No Interaction Force
- Experiment 2: $J1$ [0°] & $J2$ [3°]. No Interaction Force
- Experiment 3: $J1$ [3°] & $J2$ [3°]. Interaction Force
- Experiment 4: $J1$ [3°] & $J2$ [-3°]. Interaction Force Counteracted
- Experiment 5: $J1$ [-3°] & $J2$ [3°]. Interaction Force Counteracted

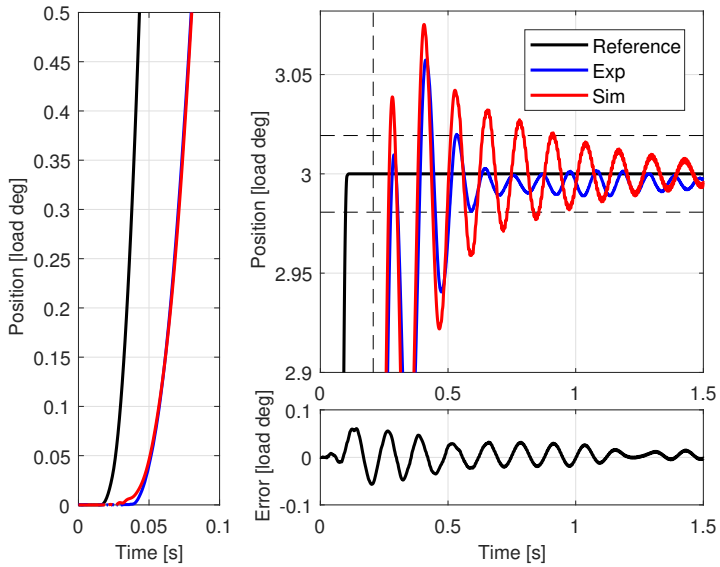

Figure 4.4: First axis load position response reproducibility

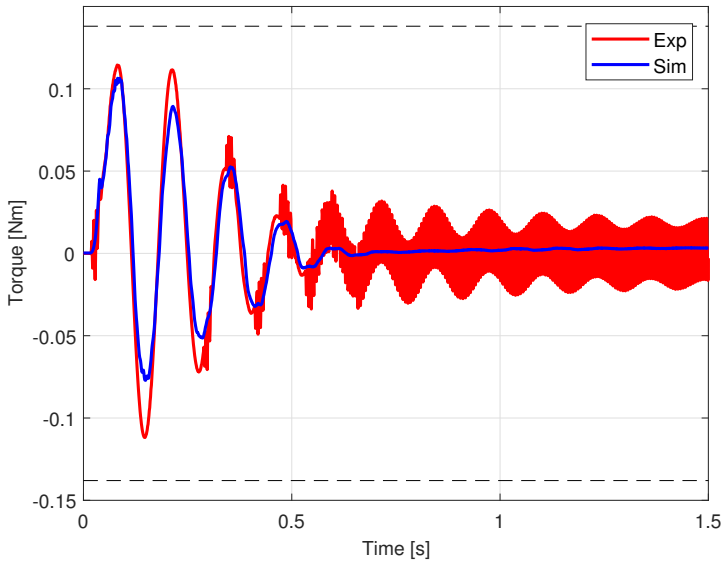

Figure 4.5: First axis Torque Command reproducibility

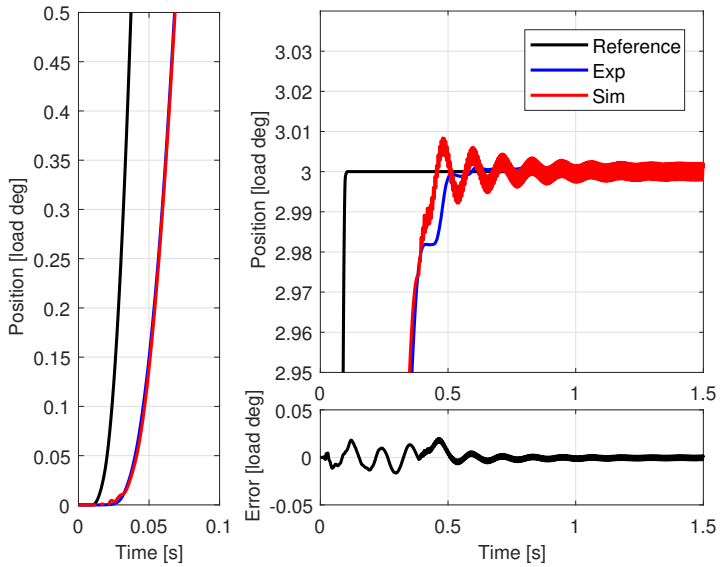

Figure 4.6: Second axis motor position response reproducibility

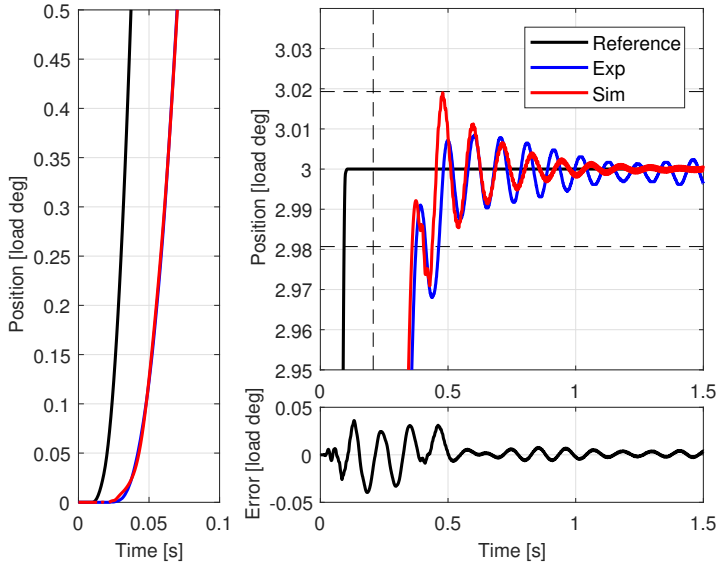

Figure 4.7: Second axis load position response reproducibility

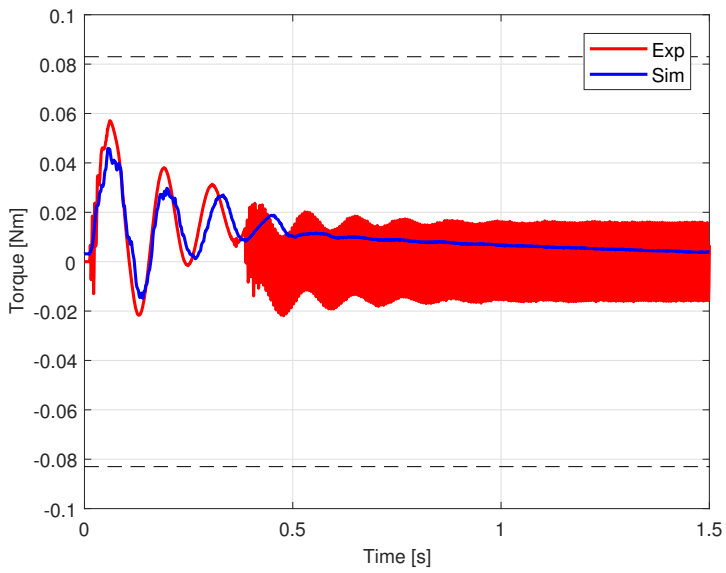

Figure 4.8: Second axis Torque Command reproducibility

Chapter 5

Controllers Development

The objective of this section is to develop multiple control methods in order to improve: speed, positioning precision and damping performance in the horizontal two-axis robot. The characteristics and the time response of the implemented controllers will be shown. Finally, a comparison between all the controllers will be done.

5.1 Preliminary

As a preamble it is emphasised the fact that two types of loop have been used: semiclosed (using motor position information) and fullclosed (using load position information). But not only that, it has also opted to use controllers of 1 degree of freedom (feedback) and 2 degrees of freedom (feedback & feedforward). As a final point to this chapter, a different approach to the problem will be shown by introducing a compensator, the Lead Compensator. Its superiority will be demonstrated by comparing it with the controllers.

5.1.1 Performance Requirements

Denso Corporation needs to provide the industry with high performance robots. Hence it asked Professor Iwasaki's laboratory for help. In this case, for the simplified SCARA robot, they need a controller capable of satisfying the following specifications:

- Settling Accuracy: ± 0.0193 [load deg]. ± 0.1 mm in terms of position conversion at the tip of the shaft
- Settling Time: 0.1 [s]

5.1.2 Experiments 1 & 2

Of the five possible experiments in which to test the controllers the 1 & 2 were selected. These two were chosen because in neither of them does the interference force between axes appear, making the controller simpler. In experiment 1, $J1$ moves from $0°$ to $3°$ while $J2$ remains servo-locked at $0°$. In experiment 2, $J2$ moves from $0°$ to $3°$ while $J1$ remains servo-locked at $0°$.

5.1.3 Starting Point. P-PI Denso Controller. Feedback Gain Design of Control System

By the way, it should be noted that *Denso Corporation* provided the P-PI Controller used, already described in section 2.1.3. Proportional of Position and Proportional and Integral of Speed. The generic block diagram can be seen in Figure 2.5. This basic scheme is the one that will be used in the following controllers. The design and gain values of this P-PI controller were supplied by *Denso Corporation*. K_{pp}, K_{vp} and K_{vi}.

5.2 1 DOF Semiclosed

In this section, it is explained and tested the cascade semi-closed control system provided by *Denso Corporation*. It is common to use a semi-closed control system, with the position information coming from the motor shaft, for positioning control of an industrial robot. However, in the semi-closed control system, the positioning accuracy of the load may be deteriorated due to friction existing in the arm mechanism or nonlinear errors of the structural

part as described in the section 2.2. Figure 5.1 shows the block diagram of the cascade semi-closed control system. In the figure, $C_p(s)$ is the position control system, $C_v(s)$ is the speed compensator, $P(s)$ is the controlled object, τ is the torque signal, S is a derivative block, ω is the angular velocity, θ_l and θ_m are the load and motor angular position and r is the position reference. The values of the compensators $C_p(s)$ and $C_v(s)$ are obtained from Table 2.3. The controlled object $P(s)$ uses the mathematical expression model constructed in section 3.3.

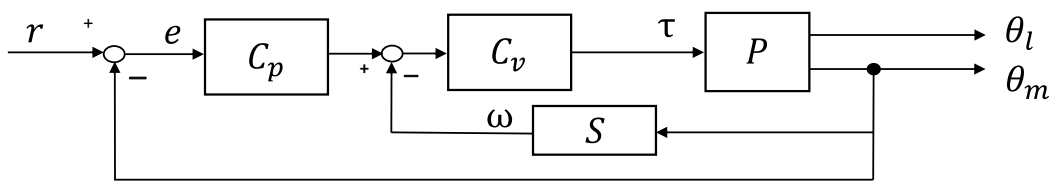

Figure 5.1: Block Diagram of 1DOF Semi-closed Control System

The cascade semi-closed controller is mounted on the actual machine and the positioning experiment is carried out. Experimental results are evaluated in order to verify its effectiveness. Figures 5.2 and 5.3 show experimental and simulated waveforms of motor position response, load position response, and torque command when the angle command designed in section 4.2 is given to one axis. On the first axis and the second axis, respectively.
As it was explained in section 4.4, in the figures, the black line represents the reference obtained in section 4.2. The blue line represents the experimental results. The red line represents the controller´s simulation. The horizontal black dot line in the position response diagram is the target settling range ±0.0193 [load deg]. The vertical black dot line is the target after 0.1 [s], which is the settling time. And finally, the horizontal black spot line in the torque command diagram shows the motor limit torque capacity.
The following table 5.1 shows the time characteristics of the controller. In the simulation there is no position error. However, there it is in the experimentation. This is because the position loop is taking the information from the motor side instead of the load side. It also has a very slow rising time that prevents it from accomplishing the main requirement: the settling time. After the settling there are still residual vibrations of 9.7 Hz, corresponding to the first mode of vibration and which must be reduced. It should also be noted that the chattering in the torque is due to the Coulomb friction implemented in the model. This last part is produced by the effects of the simulation that do not affect the experimentation. Therefore, it is not necessary to take into account and correct the chattering.

5.3 1 DOF Fullclosed

1 DOF Fullclosed is the second controller implemented. On this case, the motor information has been changed by the load information in the main loop for the purpose of correcting the steady state error. Fig. 5.4 shows the block diagram of 1DOF full-closed control system.

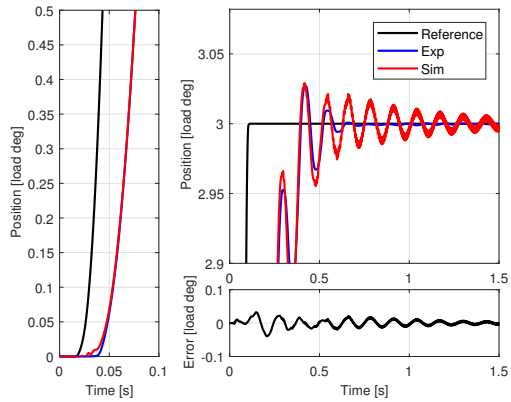

(a) J1 Motor Time Response

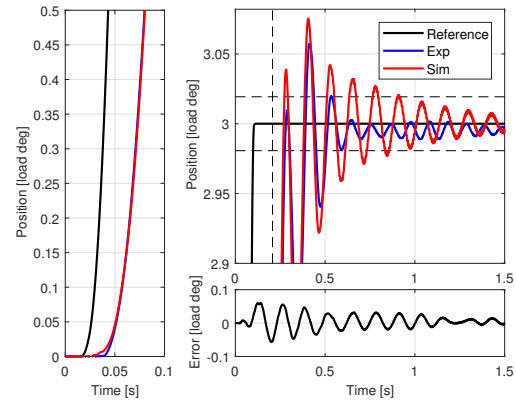

(b) J1 Load Time Response

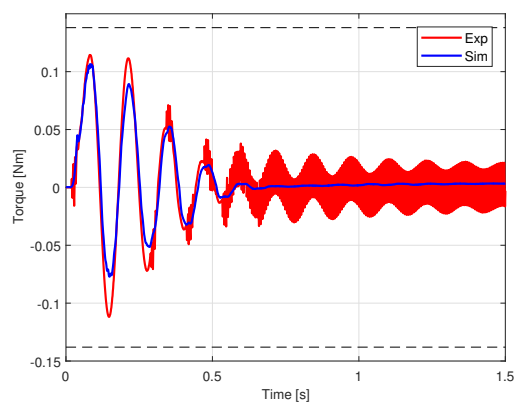

(c) J1 Torque Time Response

Figure 5.2: Experimental results (0 to 3° [load deg]) by the first-axis 1DOF semi-closed control system

The cascade semi-closed controller is mounted on the actual machine and the positioning experiment is carried out. Experimental results are evaluated in order to verify its effectiveness. As it can be seen in the Table 5.2, thanks to the full-closed control system the steady state error in the experimentation has been suppressed. However, the speed of the system remains just as slow. Therefore, improvements in the controller are still necessary.

5.4 2 DOF Semiclosed. Feedforward compensator based on irreducible decomposition expression

2 DOF Semiclosed is the third controller implemented. In light of the inability of the previous controllers to accomplish the specifications established by Denso, it is necessary to implement

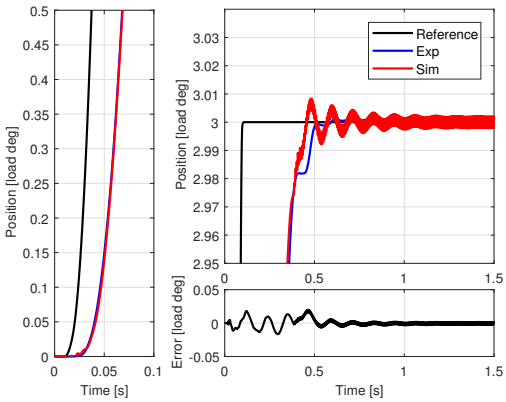

(a) J2 Motor Time Response

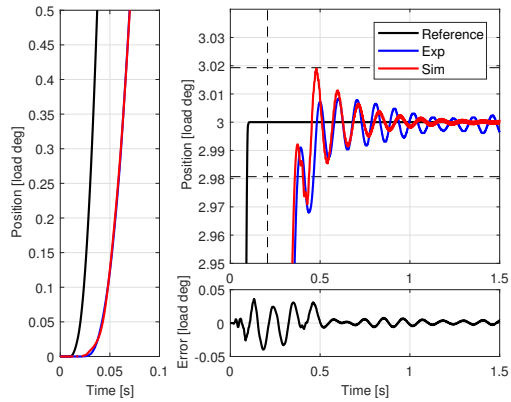

(b) J2 Load Time Response

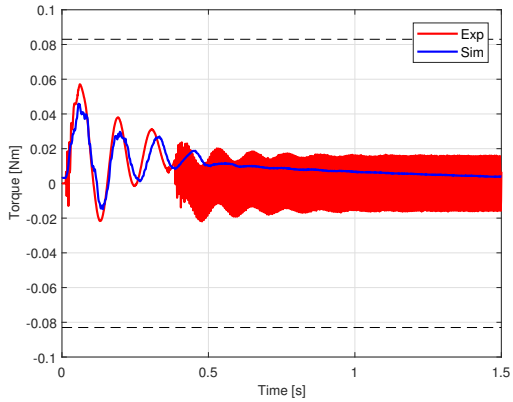

(c) J2 Torque Time Response

Figure 5.3: Experimental results (0 to 3° [load deg]) by the second-axis 1DOF semi-closed control system

a second degree of freedom in the controller: feedforward. In the conventional 1DOF control system, stability and response are all dependent on the feedback compensator. Therefore, a parameter design considering both is necessary. On the other hand, in the two-degree-of-freedom control system, the feedforward compensator guarantees quick response while the stability can be independently designed by the feedback compensator. So the application of the 2 DOF control system speeds up response and improves the control performance. On this occasion a feedforward has been implemented based on the expression of irreducible decomposition. Its design is obtained by reducing the model of the control object to the first vibration mode. A semi-closed 2 DOF control system is shown in Figure 5.7. In the figure, r is a position command, r' is a feedforward command, N_m (s), N_l (s), D(s) are feedforward compensators, C_p(s) is a position control system, C_v speed control system, and P(s) is the

Table 5.1: Comparison between experiments and simulations 1 DOF semi-closed control system

	Steady State Error	Settling Time	Rising Time	Torque Saturation
Simulation	O	X	X	O
Experiment	X	X	X	O

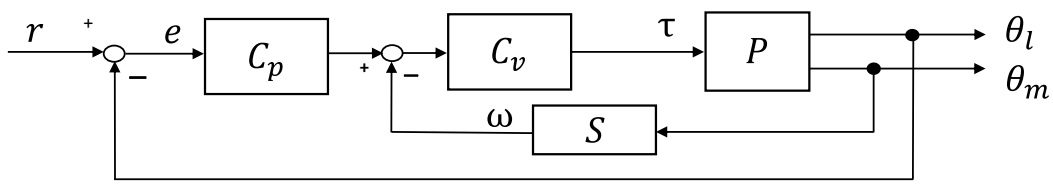

Figure 5.4: Block Diagram of 1DOF Full-closed Control System

object to be controlled.
The design method of the feedforward compensator based on irreducible decomposition expression is shown below. The transfer characteristic from the torque in the semi-closed control system to the motor position and from the torque to the load position is expressed using P_m(s) and P_l(s) in the eq. 5.1.

$$P_m(s) = \frac{P_{N_m}(s)}{P_D(s)}, P_l(s) = \frac{P_{N_l}(s)}{P_D(s)} \tag{5.1}$$

Here, the transfer function from the position command r to the motor position θ_m is expressed by the eq. 5.2.

$$\frac{\theta_m}{r} = \frac{P_{N_m}(s)(D + N_m C_p C_v + N_m C_v)}{P_D(s) + P_{N_m}(s) C_p C_v + s P_{N_m}(s) C_v} \tag{5.2}$$

At this time, in the semi-closed feedback control system, each feedforward compensator is:

$$N_m(s) = \frac{P_{N_m}(s)}{F_c(s)}, N_l(s) = \frac{P_{N_m}(s)}{F_c(s)}, D(s) = \frac{P_D(s)}{F_c(s)} \tag{5.3}$$

the transfer function from the position command r to the motor position θ_m is:

Table 5.2: Comparison between experiments and simulations 1 DOF full-closed control system

	Steady State Error	Settling Time	Rising Time	Torque Saturation
Simulation	O	X	X	O
Experiment	O	X	X	O

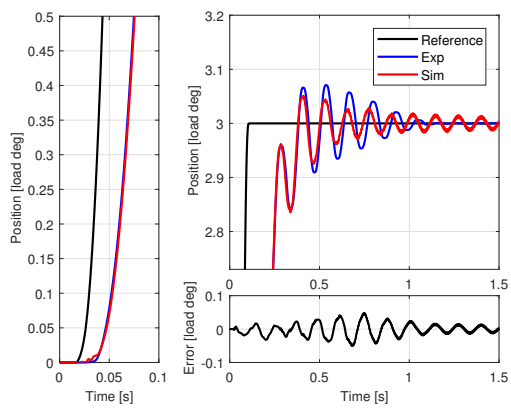

(a) J1 Motor Time Response

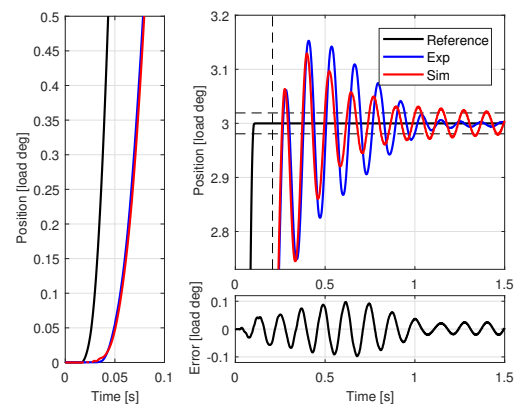

(b) J1 Load Time Response

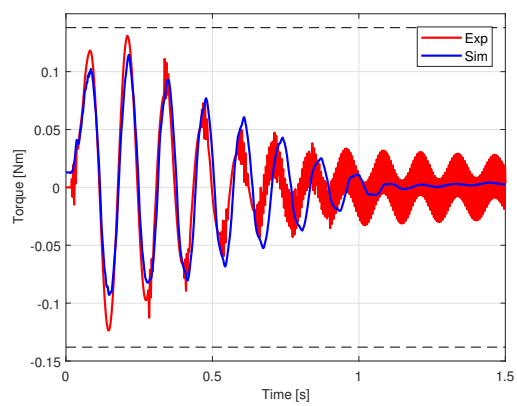

(c) J1 Torque Time Response

Figure 5.5: Experimental results (0 to 3° [load deg]) by the first-axis 1DOF full-closed control system

$$\frac{\theta_m}{r} = \frac{P_{N_m}(s)}{F_c(s)} \tag{5.4}$$

And the tracking characteristic can be arbitrarily determined by F_c. Here, F_c is a filter, a low-pass filter shown in the eq. 5.5

$$F_c(s) = (\frac{\omega_c}{s + \omega_c})^4 \tag{5.5}$$

where $F_c = \omega_c 2\pi$ [Hz].
Here, the cutoff frequency of the low-pass filter was set to 40 Hz to ensure sufficient follow-up performance. From the above equation, each feedforward compensator is derived from the transfer characteristic of the controlled object. However, in this system, since the vibration

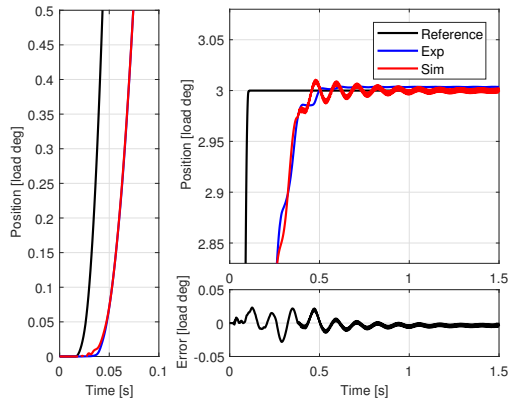

(a) J2 Motor Time Response

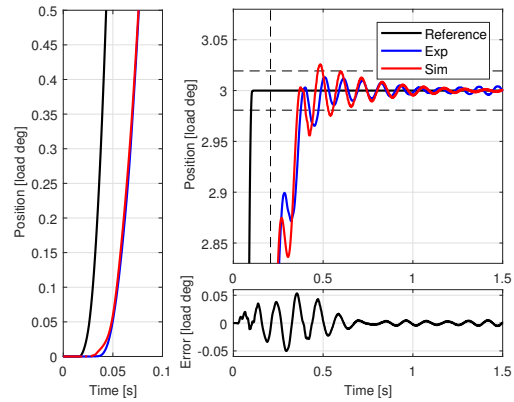

(b) J2 Load Time Response

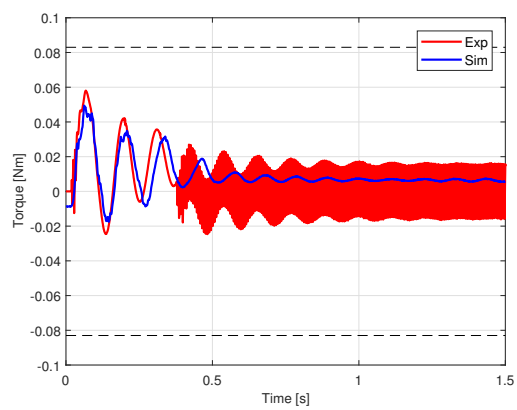

(c) J2 Torque Time Response

Figure 5.6: Experimental results (0 to 3° [load deg]) by the second-axis 1DOF full-closed control system

in the primary vibration mode is dominant in the load position response, the feedforward compensator is designed by lowering the control object only to the primary vibration mode. Figures 5.8 and 5.9 show the transfer characteristics of the feedforward compensators for the first axis and the second axis designed in the semi-closed feedback control system, respectively. The cascade semi-closed 2DOF controller is mounted on the actual machine and the positioning experiment is carried out. Experimental results are evaluated in order to verify its effectiveness.

As it can be seen in the table 5.3, a steady state error reappears in the experimentation. As previously stated, this is due to using a semi-closed loop. On the other hand, the inclusion of feedforward provides a faster response and decreases residual vibration, even though the torque saturates. It is convenient to avoid the saturation of the torque because it is used in

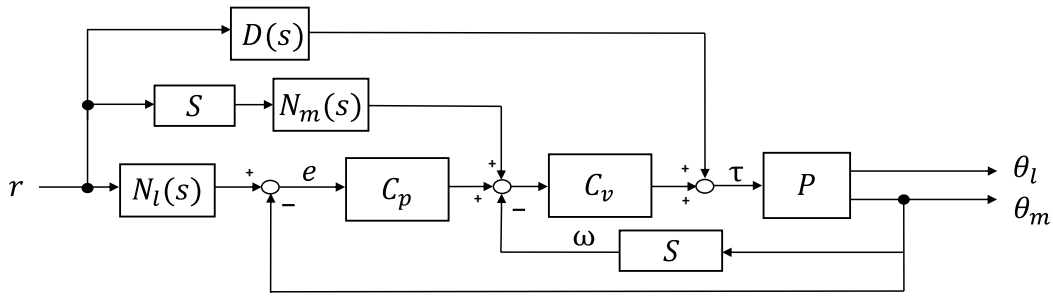

Figure 5.7: Block Diagram of 2DOF Semi-closed Control System applying FF compensator based on irreducible decomposition

the feedforward. Saturation prevents the generation of the needed torque to suppress residual vibration.

Table 5.3: Comparison between experiments and simulations 2 DOF semi-closed control system

	Steady State Error	Settling Time	Rising Time	Torque Saturation
Simulation	O	X	O	O
Experiment	X	X	O	O

5.5 2 DOF Fullclosed

2 DOF Fullclosed is the last implemented controller. 2 DOF semiclosed controller brought a great improvement in the behaviour of the robot. However, it was not enough because the load still had a steady state error. So a modification was needed: a fullclosed loop, as was previously done for this problem. The design method of the feedforward compensator based on irreducible decomposition expression is shown below in Fig. 5.12.
Transfer characteristics from the torque in the full closed control system to the motor position and from the torque to the load position are expressed by the following equation using P_m(s) and P_l(s) (eq. 5.1). Here, the transfer function from the position command r to the load position θ_l is expressed by the equation 5.6.

$$\frac{\theta_l}{r} = \frac{P_{N_l}(s)(D + N_l C_p C_v + N_m C_v)}{P_D(s) + P_{N_l}(s) C_p C_v + s P_{N_m}(s) C_v} \tag{5.6}$$

At this time, in the full-closed feedback control system, each feedforward compensator is:

$$\frac{\theta_l}{r} = \frac{P_{N_l}(s)}{F_c(s)} \tag{5.7}$$

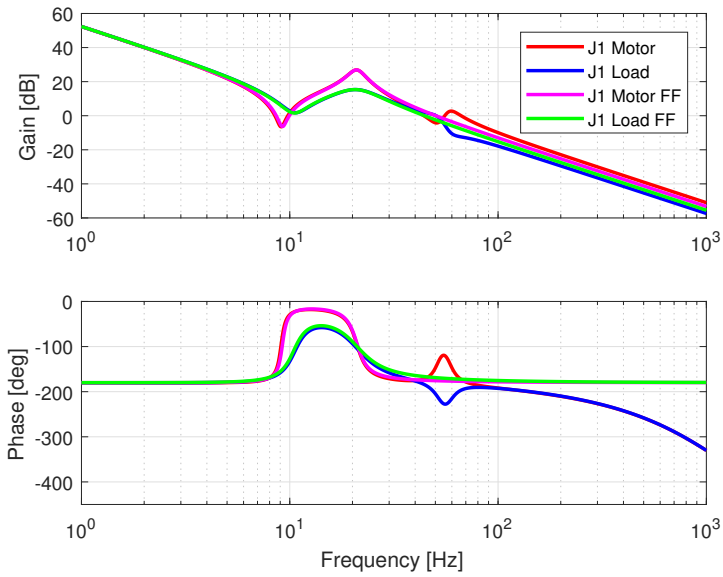

Figure 5.8: Transmission characteristic of the feedforward compensator of the first axis (semi-closed control system)

The tracking characteristic can be arbitrarily determined by F_c. Here, as in section 5.4, F_c is set to a low pass filter of 40 [Hz] to ensure sufficient follow-up performance, and F_c is fully closed. In the control system as well, the feedforward compensator is designed by lowering the control target to only the primary vibration mode. Figures 5.13 and 5.14 show the transfer characteristics of the 1st and 2nd axis feedforward compensators designed in the full-closed feedback control system (5.8 and 5.9).
The cascade semi-closed 2DOF controller is mounted on the actual machine and the positioning experiment is carried out. Experimental results are evaluated in order to verify its effectiveness.
Table 5.4 shows that there is no steady state error. A fast response and low residual vibration are obtained. However, the system is still not able to meet the Denso requirements and also the torque saturates in the experiment.

Table 5.4: Comparison between experiments and simulations 2 DOF semi-closed control system

	Steady State Error	Settling Time	Rising Time	Torque Saturation
Simulation	O	X	O	O
Experiment	O	X	O	O

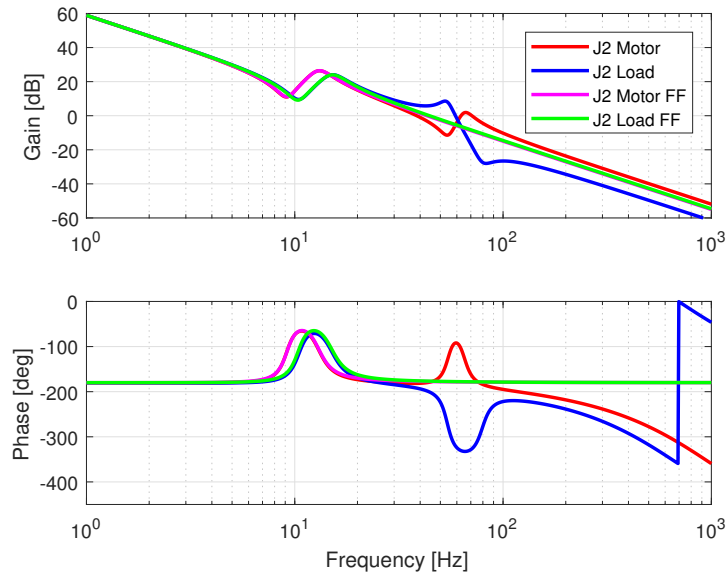

Figure 5.9: Transmission characteristic of the feedforward compensator of the second axis (semi-closed control system)

5.6 Lead Compensator

After seeing the invalidity of the proposed controllers to meet the specifications, it was opted for a new approach to the problem. It was decided to follow the criterion of selection and design of controllers and compensators from the engineering course of Automatic Regulation from Castilla-La Mancha University(Spain). A flowchart showing the controllers selection process can be seen in FigureC.1 from AnnexC. In this case:

1. Set system specifications: t_s, t_p, t_r, M_p, ξ, ω_n, steady state error (s.s.e). For the horizontal two-arm robot: t_s=0.01 [s], s.s.e=0.
2. Calculate the position of the poles. s=-$\omega_n(\xi \pm \mathrm{i}\sqrt{1-\xi^2})$
3. Check the Root Locus with a P-type regulator.
4. Since the pole is not in Root Locus, calculate $\xi_c > 0$.
5. Since $\xi_c > 0$, it is decided to design a Lead Compensator.

The Lead Compensator is a regulator used to improve the phase margin of the system, that is, to improve its relative stability and increase its velocity response. This compensator lowers the gain at low frequencies, increases it at high frequencies and raises the phase angle of the total average frequency. Which is relative to the cutoff frequency determined by the time constant T. To compensate for the loss gain produced, it is common to apply a gain

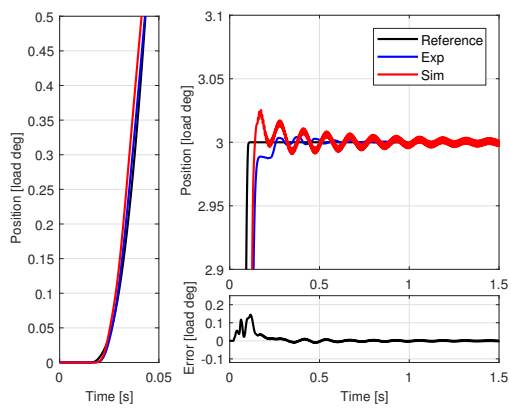

(a) J1 Motor Time Response

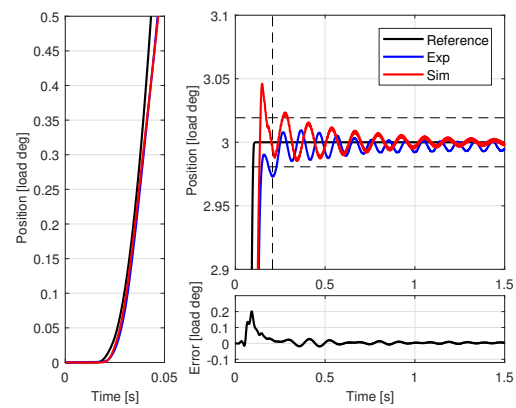

(b) J1 Load Time Response

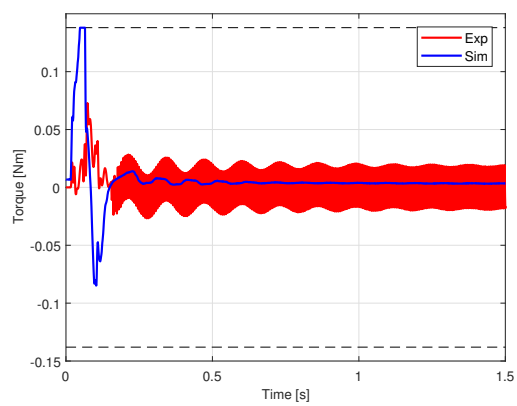

(c) J1 Torque Time Response

Figure 5.10: Experimental results (0 to 3° [load deg]) by the first-axis 2DOF semi-closed control system

compensation. By correctly adjusting the previous parameters, the place of the roots can be moved to the left half-plane in order to increase the system bandwidth and, therefore, the velocity response.
A high gain crossover frequency means higher bandwidth and faster response. However, if there are noisy signals present, an excessively large bandwidth is not desirable, as this makes the system more susceptible to noise signals. Since there is an increase in gain at high frequencies.
The following block diagram shows its implementation in the robot:
The lead compensator is characterised by:

- Possess a real pole and a real zero.
- The zero is closer to the origin $w_z < w_p$.

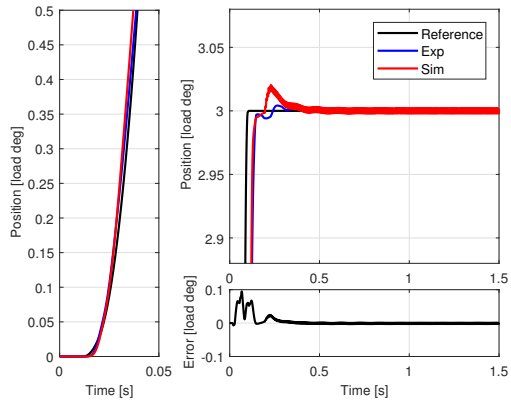

(a) J2 Motor Time Response

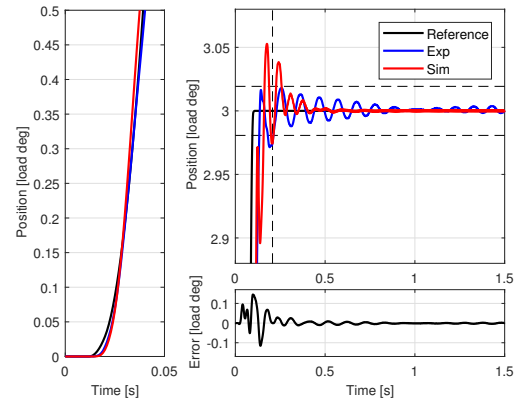

(b) J2 Load Time Response

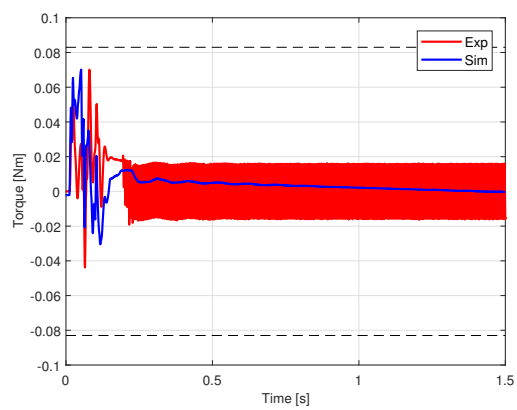

(c) J2 Torque Time Response

Figure 5.11: Experimental results (0 to 3° [load deg]) by the second-axis 2DOF semi-closed control system

- Its generic transfer function is: $\frac{\omega_p}{\omega_z}\ \frac{s+\omega_z}{s+\omega_p}$

This new approach specifies the performance of the transient response in an indirect way. That is, in terms of phase margin, gain margin and magnitude of the resonance peak. These values provide a rough estimate of the velocity of the transient response and the static error constants, which provide steady state accuracy.

$$Rs'(s) = K\frac{(s+z_1)(s+z_2)}{(s+p_1)(s+p_2)}, \quad |z_2| < 0.1d \tag{5.8}$$

To design the Lead Compensator part, first, the most appropriate values of phase margin and gain cross-over frequency were selected by trial and error:

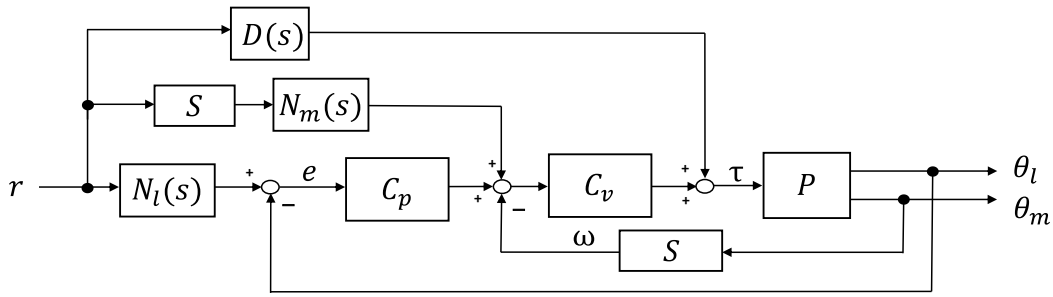

Figure 5.12: Block Diagram of 2DOF Full-closed Control System applying FF compensator based on irreducible decomposition

$$M_f = 74 \times \frac{pi}{180} \qquad \text{Phase Margin}$$

$$w_g = 50 \qquad \text{Gain Cross-over frequency}$$

Then, the necessary values were obtained to define the Lead Compensator, with the following equations:

$$R_j w = -\frac{e^{M_f i}}{freqresp(Gs_{J1_c}, \omega_{gj})}$$

*freqresp corresponds to the entire frequency response of the system

$$Mod_R = |R_i \omega|$$

$$Fas_R = \angle R_i \omega$$

$$f_L = \frac{1 - \sin(Fas_R)}{1 + \sin(Fas_R)}$$

$$f = 0.0071$$

$$x = \frac{1 - f - \sqrt{(1-f)^2 - 4\,f\,tan(Fas_R)^2}}{2\,f\,tan(Fas_R)}$$

$$T = \frac{x}{\omega_g}$$

$$K = Mod_R \sqrt{\frac{1 + f^2\,x^2}{1 + x^2}}$$

$$R_s = \frac{K(1 + T\,s)}{1 + f\,T\,s} \tag{5.9}$$

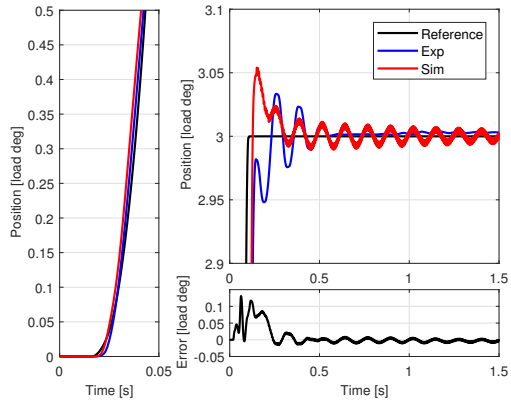

(a) J1 Motor Time Response

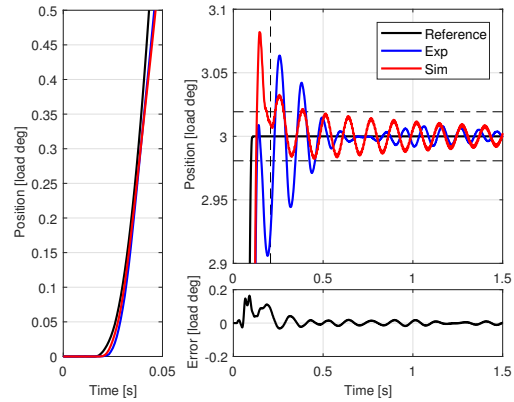

(b) J1 Load Time Response

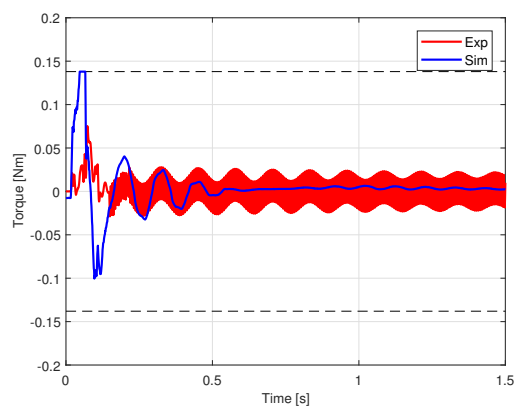

(c) J1 Torque Time Response

Figure 5.13: Experimental results (0 to 3° [load deg]) by the first-axis 2DOF full-closed control system

5.7 Comparison

In the figures 5.17, 5.18 and 5.19 the black line represents the reference obtained in section 4.2 and the other colours represent the simulations. The blue line represents the semi-closed 1DOF controller. The red line represents the semi-closed 2DOF controller. The green line represents the full-closed 1DOF controller. The blue line represents the full-closed 2DOF controller. Finally, the magenta line represents the Lead Compensator. As can be seen in figures 5.17, 5.18 and 5.19, controllers with 1DOF have the worst time response. Controllers with 2DOF have a faster and more stable response than 1DOF, but they still do not meet the specifications required by Denso Corporation. The only controller/compensator able to meet these specifications is the Lead Compensator (in the firs-axis). Also, it should be noted that for the case of J2 it has not been possible to optimise the compensator to meet the

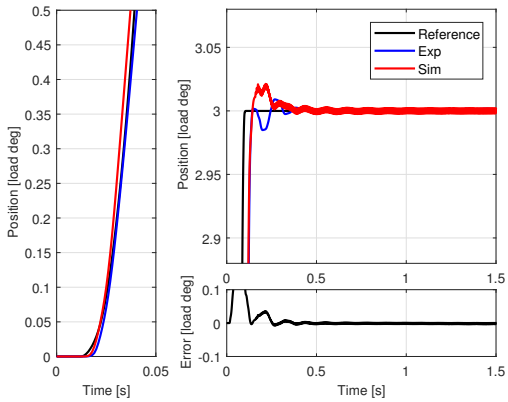

(a) J2 Motor Time Response

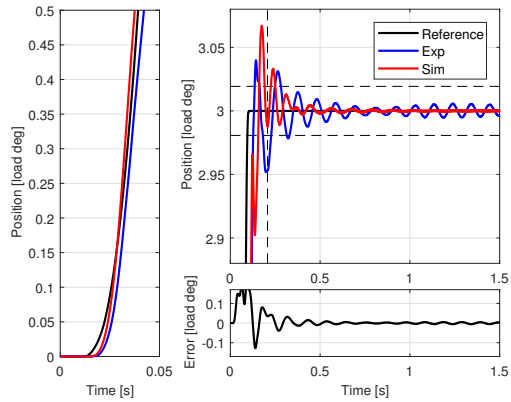

(b) J2 Load Time Response

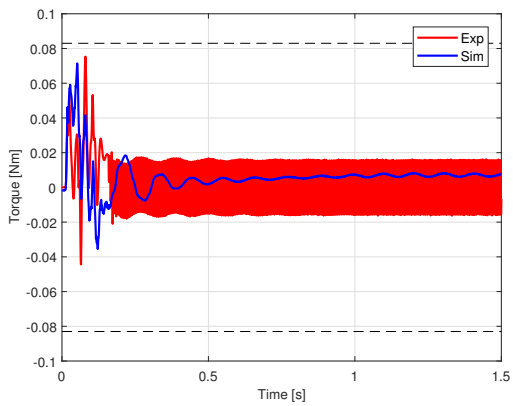

(c) J2 Torque Time Response

Figure 5.14: Experimental results (0 to 3° [load deg]) by the second-axis 2DOF full-closed control system

requirements. It is a task to be developed in the future.
The Table 5.5 shows the Lead Compensator characteristics.

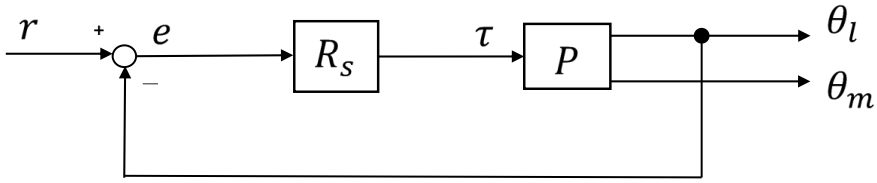

Figure 5.15: Block Diagram of the Lead Compensator

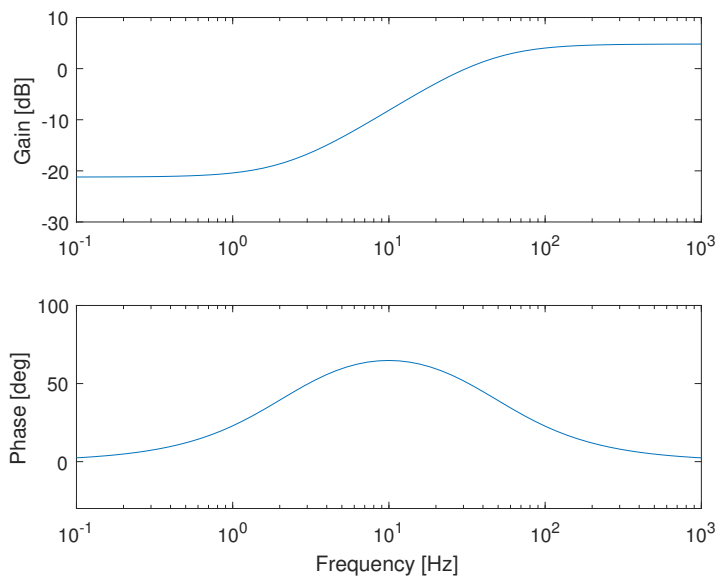

Figure 5.16: Lead Compensator Bode Diagram

Table 5.5: Lead Compensator Simulation Characteristics

	Steady State Error	Settling Time	Rising Time	Torque Saturation
Lead Compensator	O	O	O	O

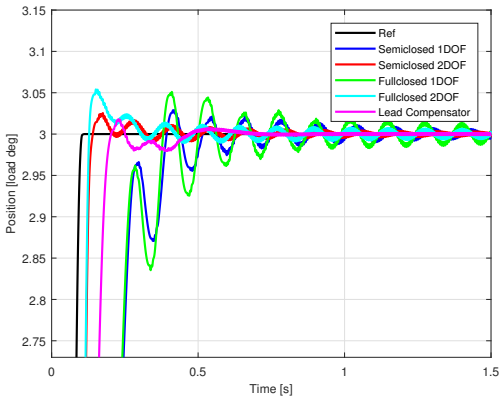

(a) J1 Motor Position Time Response(3°)

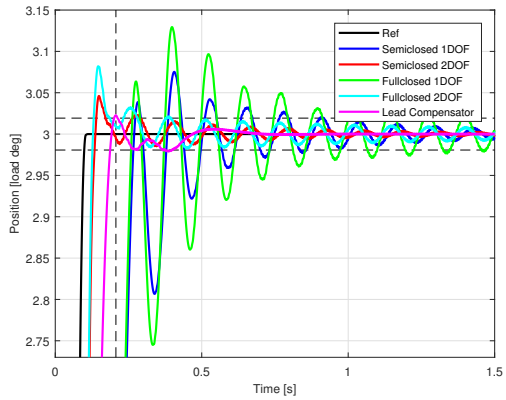

(b) J1 Load Position Time Response (3°)

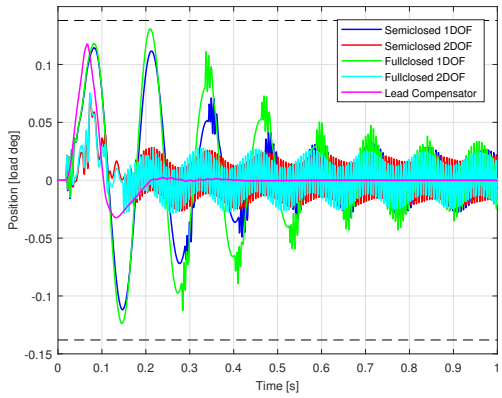

(c) J1 Torque Time Response (3°)

Figure 5.17: Comparison of simulation results (0 to 3° [load deg])by the first-axis between the different controllers and the Lead Compensator

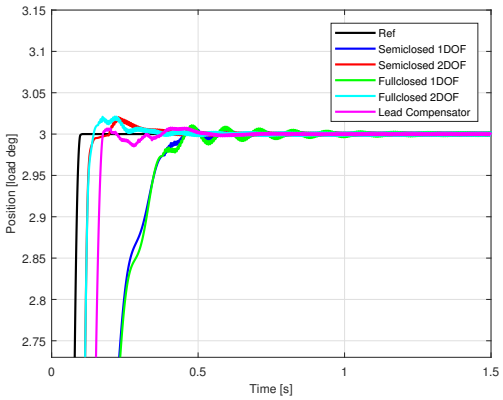

(a) J2 Motor Position Time Response(3°)

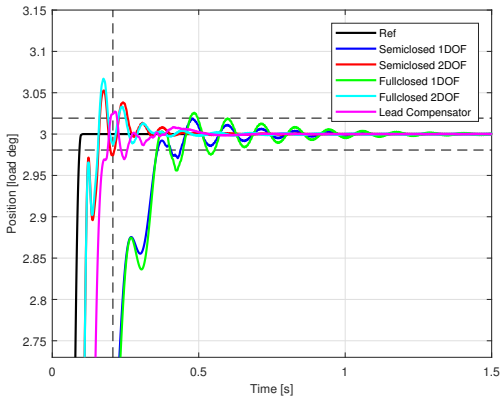

(b) J2 Load Position Time Response (3°)

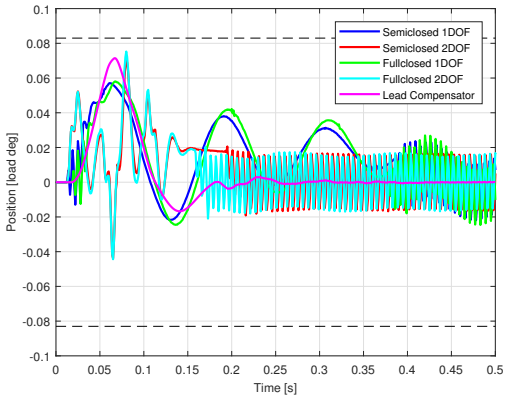

(c) J2 Torque Time Response (3°)

Figure 5.18: Comparison of simulation results (0 to 3° [load deg])by the second-axis between the different controllers and the Lead Compensator

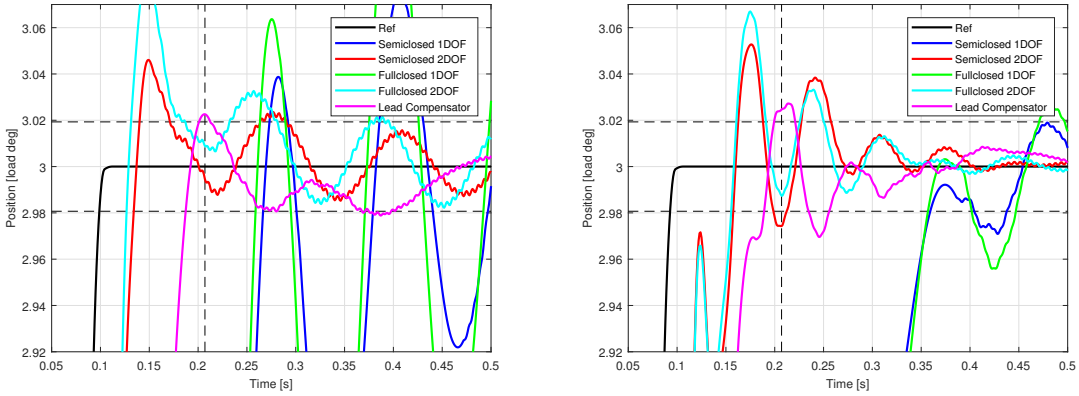

(a) J1 Load Position Time Response(3°)

(b) J2 Load Position Time Response (3°)

Figure 5.19: Zoom in the load time response comparison of simulation results (0 to 3° [load deg]) by the first and second-axis between the different controllers and the Lead Compensator

Chapter 6

Inter-axis Interference Force

Chapter 6 explains the interaction force in the equipment under test. Experiments are carried out and conclusions are drawn.

6.1 Introduction

The final objective of this research team is to construct a damping control system for an industrial four-axis horizontal scalar robot, and use it by operating multiple axes at the same time, not a single axis at the time of use. When multiple axes are moved at the same time, appears a new phenomenon not yet taken into account: the inter-axle interference force. Each axis brings an extra torque to the rest and vice versa. This interference torque must be taken into account and attenuated. Since the positioning performance is greatly deteriorated by the inter-axis interference force generated at that time, this chapter verifies the influence of this inter-axis interference force when the horizontal two-axis robot arm is simultaneously driven with two axes.

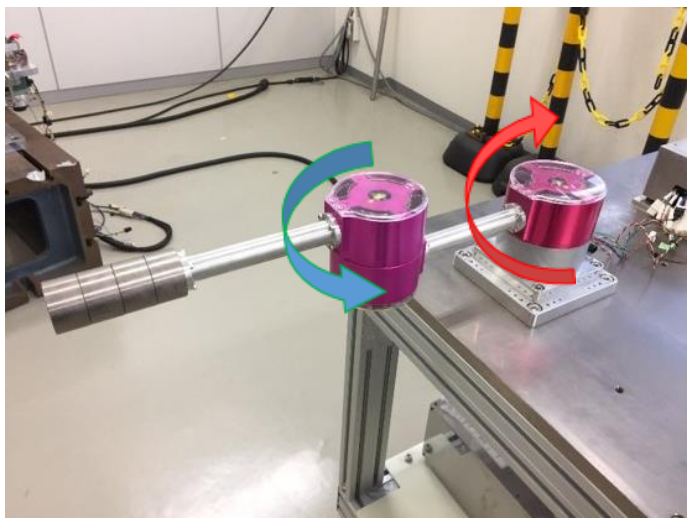

Figure 6.1: Interference Forces in the Horizontal Two-Axes Robot Arm

Fig. 6.1 shows the experiment 1 for 1 DOF semi-closed: J2 has a reference of 0°, this means, servolocked. However, the driving conditions of J1 are set from 0 to 3° [load deg] at which the vibration of each axis becomes the largest. This generates a disturbance on J2. The J2 controller attempts to correct these disturbances. It is clarified the inter-axis interference force and in what kind of frequency band influences by checking the torque command value in the servolocked axis. It can be seen that the frequency component of the vibration due to the inter-axis interference force exists in the vicinity of 9.5 Hz.

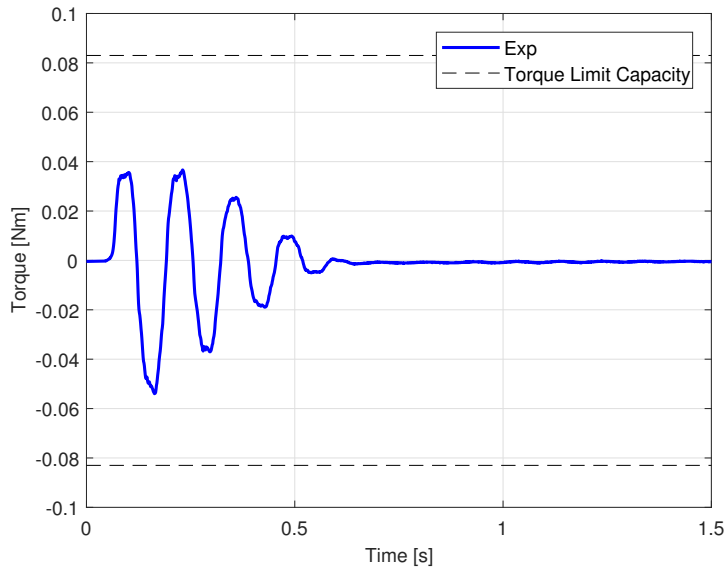

Figure 6.2: Vibrations due to J2 Torque 1st Experiment. J1 moves to 3 degrees and J2 Servolocked

6.2 Comparison Time Response Experiments

Several experiments were carried out with each of the controllers designed (1DOF semi-closed, 1DOF semi-closed, 2DOF semi-closed & 2DOF full-closed) to compare the time response of one arm while the other one executes different types of movements. In section 6.2 will be shown the case of 1DOF Semiclosed controller. In Figure 6.3,a ,b and c the behaviour of J1 is shown moving from 0 to 3° while the movement of J2 is varied. The black line represents the reference designed in section 4.2. The blue line indicates that J2 remains servolocked. The red one that J2 also moves from 0 to 3°. And finally, the green line indicates that J2 moves from 0 to -3°.

Figures 6.4a, b, c show the behaviour of J2 for different references is shown while J1 moves from 0° to 3°. On this case, it was necessary to create a relative reference to compare the different results. In one case J2 is maintained at 0°, in the other one moves 3° and in the last one -3°. In order to compare, offsets were added. When J2 moves positive 3° an offset of -3° is added, thus J2 is set to 0°. When J2 moves 3° negative an offset of +3 is added, so J2 ends at 0° as well. Once the three cases are set to 0°, their behaviours can be compared. After analysing the six figures it is observed that each axis greatly vibrates at the time of simultaneous two-axis moving in the same direction. In other words, the worst case to control is in which the axes move from 0 to 3° simultaneously. Therefore, this is the case in which is needed to work on. The rest of the graphs with the other controllers are in the appendix B.

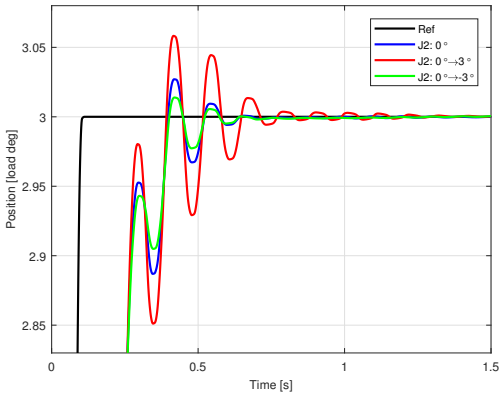

(a) J1 Motor Position Response (3°) Affected by J2 Movement

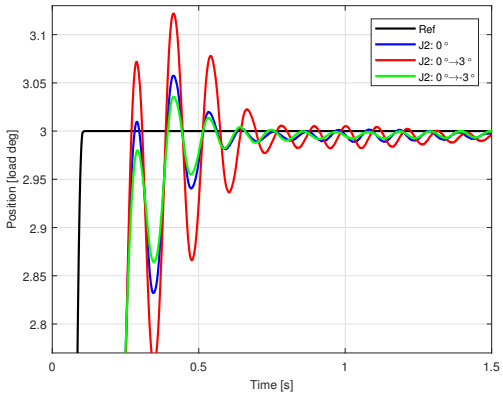

(b) J1 Load Position Response (3°) Affected by J2 Movement

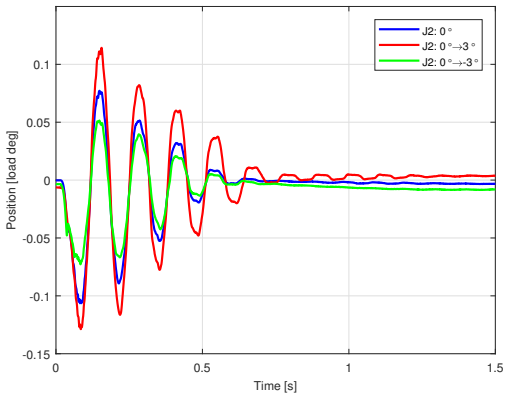

(c) J1 Torque Response (3°) Affected by J2 Movement

Figure 6.3: J1 Response with J2 Interaction Semiclosed 1 DOF

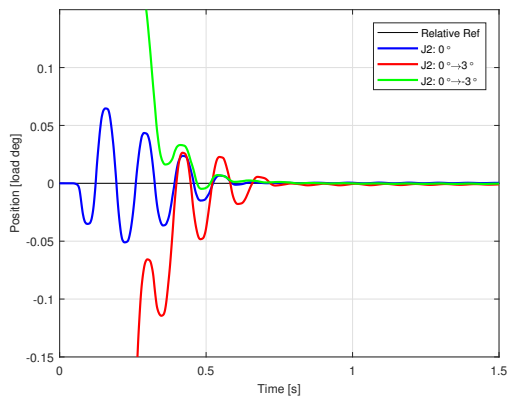

(a) J2 Motor Position Response (3°) Affected by J1 Movement

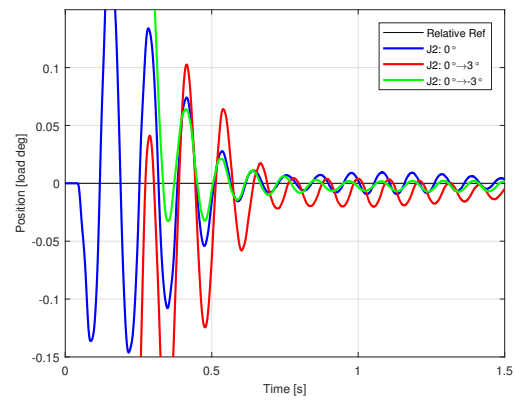

(b) J2 Load Position Response (3°) Affected by J1 Movement

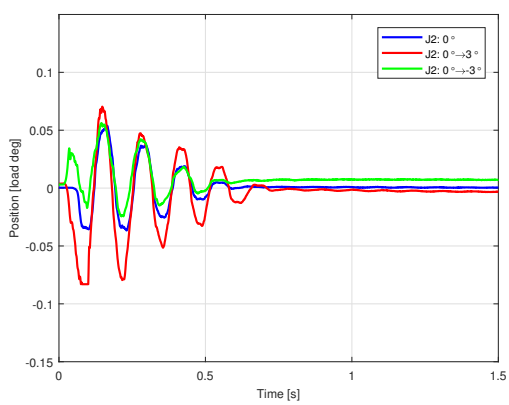

(c) J2 Torque Response (3°) Affected by J1 Movement

Figure 6.4: J1 Response with J2 Interaction Semiclosed 1 DOF

Chapter 7

Disturbance Testing Simulation

Chapter 7 deals with the Lead-Lag Compensator with disturbances to check the behaviour in simulations and a solution implemented to improve the controller.

7.1 Disturbance

The effect produced by the interference force is equivalent to adding a variable disturbance to the system at the entrance of the plant. The previously selected compensator, Lead Compensator, will be tested in this new situation. To this end, a constant torque perturbation will be added in the plant.

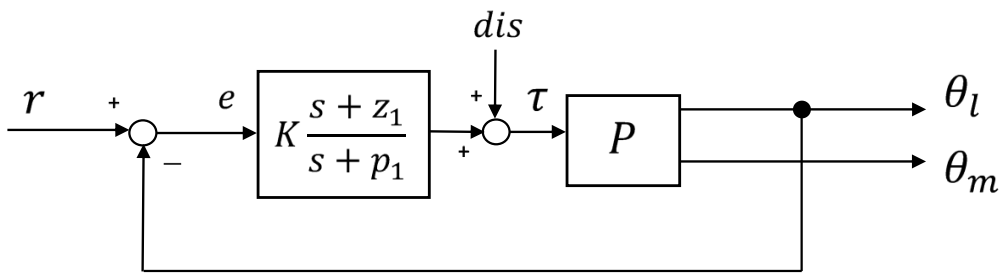

Figure 7.1: Lead Compensator Simulink Model

7.2 Lead Compensator with Disturbance

In this section, it has been decided to make a comparison among the different performances of the Lead Compensator for different situations. Figures 7.2 and 7.3 show the temporal response of J1 and J2, respectively. The black line represents the reference designed in section 4.2. The blue line represents the movement of the arm when the *disturbance=0 [mN m]*. The red line represents the movement of J1 when the *disturbance=5 [mN m]*. Finally, the magenta colour line represents the movement of J1 when the *disturbance=-10 [mN m]*. It should be mentioned that in Figures 7.2a and 7.2b the error plot represents the difference between the model and the reference. From the graphs is observed that for each perturbation unit $[mN\,m]$, 40 angular position units [°] are obtained, that is, a gain of 40 and a steady state error.

The Lead Compensator is not able to correct this error. Therefore, a new modification is necessary. Based on the flow diagram of the Appendix C. It can be seen that after choosing, designing and implementing the Lead Compensator it must be checked if there is any steady state error. However, when adding the disturbance to the entrance of the plant, the steady state error appears. To correct this error the Lead Compensator has to become a Lead Lag Compensator. In this case, it has to be added a Lag Compensator to the already designed Lead Compenstor.

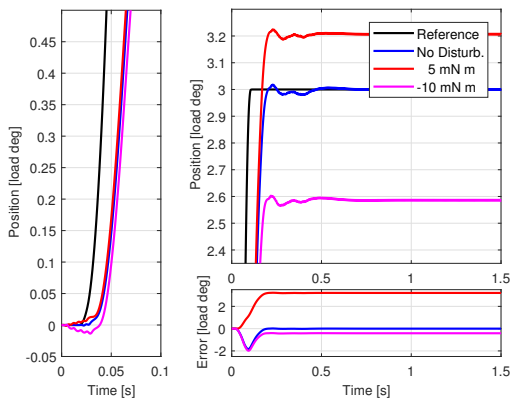

(a) J1 Motor Time Response

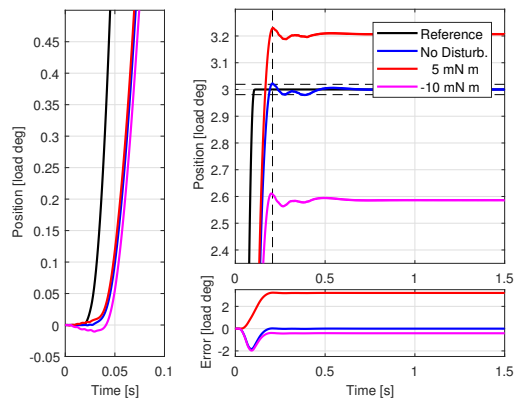

(b) J1 Load Time Response

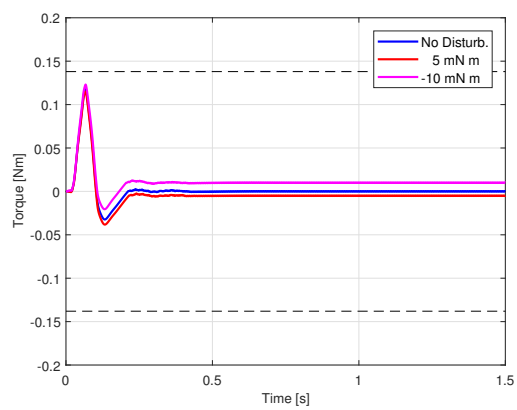

(c) J1 Torque Time Response

Figure 7.2: Simulation results (0 to 3° [load deg]) by the first-axis Lead Compensator control system

7.3 Lead Lag Compensator

Lead compensation produces, in essence, a reasonable improvement in the transient response and stability margins and a small change in steady state accuracy. But it can accentuate the effects of high frequency noise. It can be seen the certain equivalence between a Lead Compensator and a PD regulator. On the other hand, Lag compensation produces a marked improvement in the steady-state accuracy at the expense of increasing the transient response time. It suppresses the effects of noise signals at high frequencies. The Lag Compensator is equivalent to a PI regulator. Lead-Lag compensation combines the characteristics of Lead compensation with those of Lag compensation. The use of a Lead or Lag compensator increases the order of the system by 1. Using a Lead-Lag Compensator raises the order of the system by 2, which means that the system becomes more complex and more difficult to

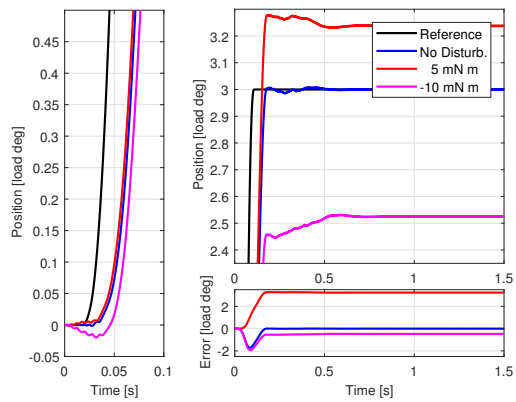

(a) J2 Motor Time Response

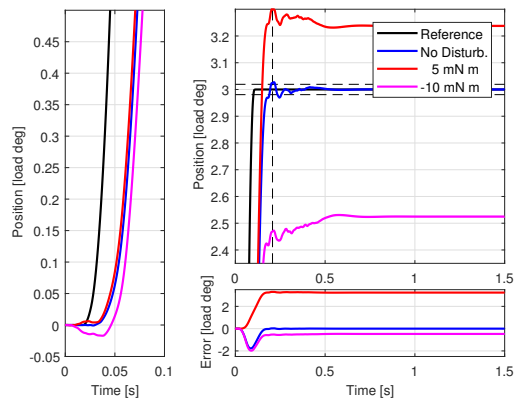

(b) J2 Load Time Response

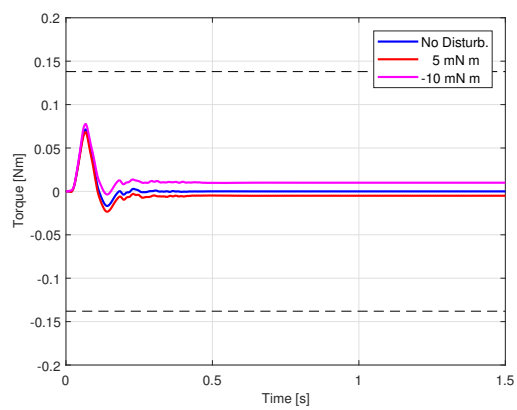

(c) J2 Torque Time Response

Figure 7.3: Simulation results (0 to 3° [load deg]) by the second-axis Lead Compensator control system

control the behaviour of the transient response. An equivalence can be observed with a PID regulator.
The Fig. 7.4 shows the Simulink Model with the Lead Lag Compensator.

$$Rs'(s) = K\frac{(s+z_1)(s+z_2)}{(s+p_1)(s+p_2)} \quad |z_2| < 0.1d \tag{7.1}$$

To design the Lead Compensator part, first, the values of phase margin and gain cross-over frequency had to be adjusted again: Phase Margin:

$$M_f = 85\frac{\pi}{180} \tag{7.2}$$

Gain Cross-over frequency:

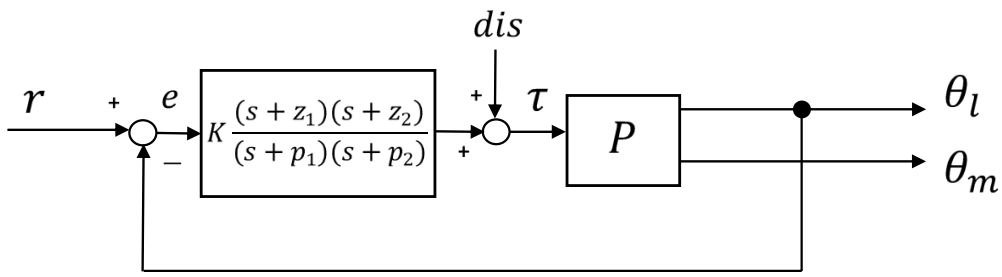

Figure 7.4: Lead Lag Compensator Simulink Model

$$w_g = 59 \tag{7.3}$$

Then, the necessary values were obtained to define the Lead Compensator, with the following equations:

$$R_j w = -\frac{e^{M_f i}}{freqresp(Gs_{J1_c}, \omega_{gj})}$$

*freqresp corresponds to the entire frequency response of the system

$$Mod_R = |R_i \omega|$$

$$Fas_R = \angle R_i \omega$$

$$f_L = \frac{1 - \sin(Fas_R)}{1 + \sin(Fas_R)}$$

$$f = 0.0071$$

$$x = \frac{1 - f - \sqrt{(1-f)^2 - 4\,f\,tan(Fas_R)^2}}{2\,f\,tan(Fas_R)}$$

$$T = \frac{x}{\omega_g}$$

$$K = Mod_R \sqrt{\frac{1 + f^2\,x^2}{1 + x^2}}$$

$$R_s = \frac{K(1 + T\,s)}{1 + f\,T\,s} \tag{7.4}$$

To design the Lag Compensator part, the most appropriate values of phase margin and gain cross-over frequency were selected by trial and error:

$$M_f = 75\frac{pi}{180} \quad \text{Phase Margin} \tag{7.5}$$

$$\omega_g = 52 \quad \text{Gain Cross-over frequency} \tag{7.6}$$

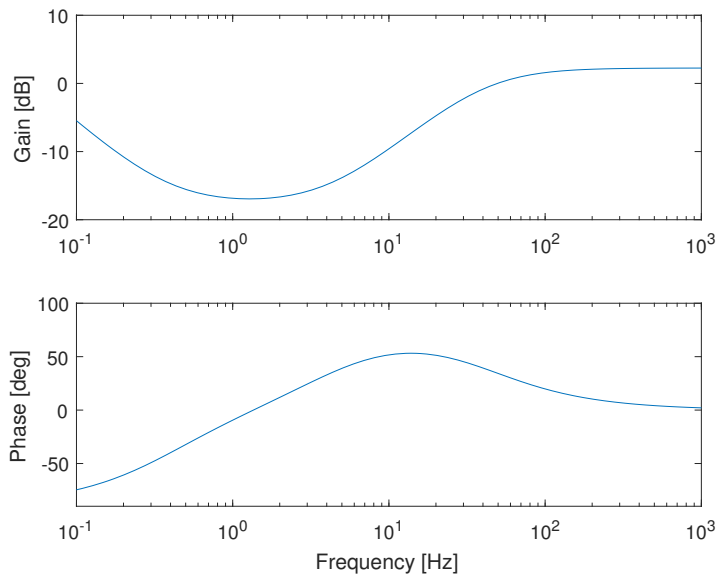

Figure 7.5: Lead Lag Compensator Bode Diagram

7.4 Time Response with Disturbance

In Figures 7.6 a and b, how the new compensator is able to correct the steady state error over time is seen. The design parameters have been obtained by trial and error. The Lead Lag Compensator is able to correct the error in the steady state but not yet fast enough. For this reason, it is necessary to optimise the design parameters, to achieve a faster response. This will be the next step of this research.

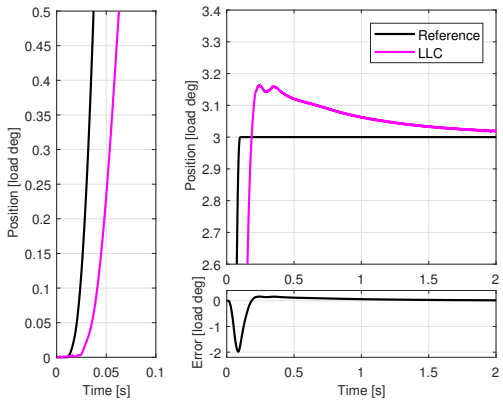

(a) J1 Motor Time Response

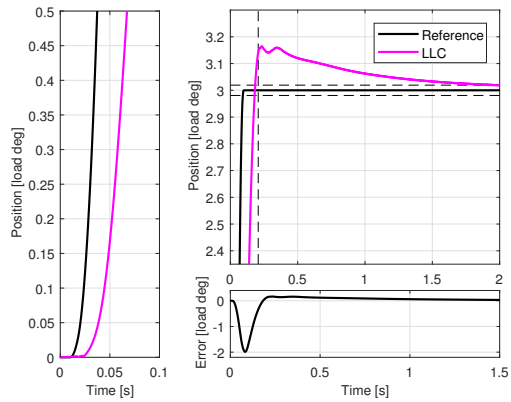

(b) J1 Load Time Response

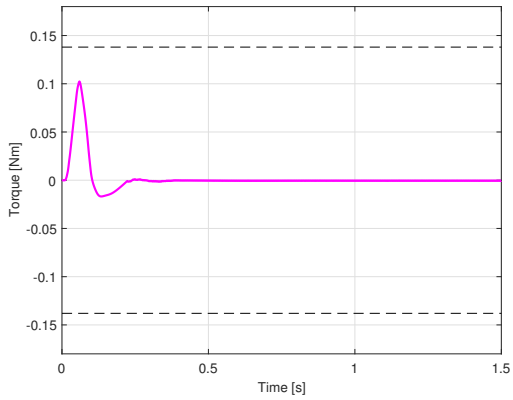

(c) J1 Torque Time Response

Figure 7.6: Simulation results (0 to 3 [load deg]) by the second-axis Lead Lag Compensator control system

Chapter 8

Conclusion

Research result and future tasks will be described.

8.1 Conclusions

- Thanks to the development of this work during 6 months of research in Japan, a better knowledge has been obtained in Control Theory
- During the development of the experiments, new functions have been implemented in Matlab. Now systems can be identified using a new simpler method or through the specialised function of Matlab
- It has moved from simple controllers with 1 DOF to more complex controllers with 2 DOF to achieve a remarkable improvement in the performance of the robot
- The worst case in which the robot can work is when $J1$ & $J2$ move to $3°$ simultaneously. This generates an interference force between the axes
- The addition of a new but simple compensator has been useful to greatly improve the performance of the system

8.2 Future Tasks

- Use the New FRA to Get a Better Frequency Characteristic from the Robot
- Use the New Identification Method with the New FRA to Get and Accurate Model
- With an Accurate Model is Possible to Get a Better Controller
- Implement an Adaptive Controller Depending on $J2$ Position Related to $J1$ (Appendix A)
- Tune and Optimise the Lead Lag Compensator
- Make Experiments with the New Controller

References

Harmonic Drive Systems. 2004.

S. O. Kazuto Imaichi. *Outer Surface of Wave Generator of Harmonic Drive Gear and Flex Mixed lubrication analysis on line inner circumference: Numerical analysis at no load torque (Mechanical elements, lubrication, machining, production control, etc.)*, volume 72. 2006.

T. Misawa. *Harmonic Drive Speed Reducers as Robotic Reducer*, volume 9. 1991.

T. Mizuno. Characteristic analysis and compensation of angular transmission error in wave gear equipment. 2008.

T. Nagamatsu. Introduction to mode analysis. 1993.

A. Noda. *Current status and problems of industrial robots*. 1990.

R. Oya. Characteristic analysis and modeling of positioning mechanism including harmonic drive gear. 2008.

Y. Sugiura, J. Kato, Y. Maeda, and M. Iwasaki. A study on frequency response analysis using friction model for frictional systems. In *Mechatronics (ICM), 2017 IEEE International Conference on*, pages 37–42. IEEE, 2017.

Y. Takizawa. *Small high-principle Harmonic Drive Gear for robots*, volume 109. 2006.

Y. Yonemoto. *Present state and future prospects of Japanese industrial robots*. 1976.

Appendix A

Sine Sweep Frequency for an Adaptive Controller

Figure A.1 shows the sine sweep frequency for an adaptive controller.

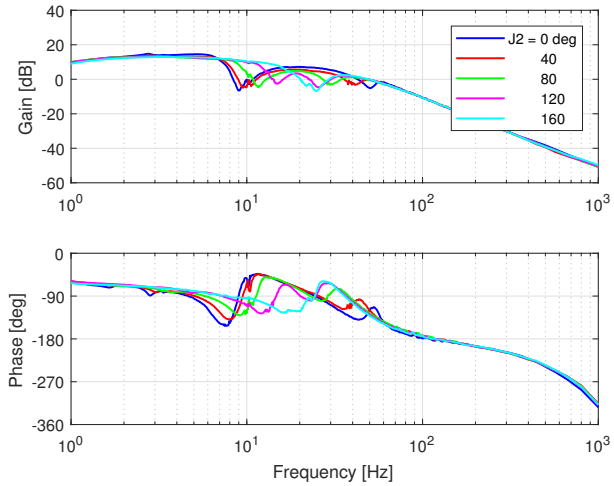

(a) J1 Motor Gain & Phase in different joint angles

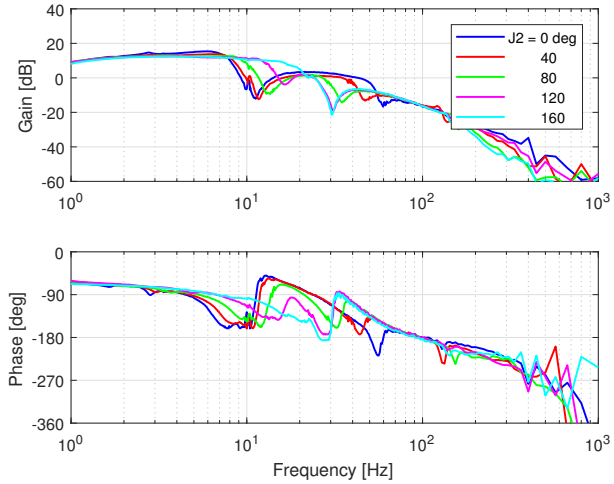

(b) J1 Load Gain & Phase in different joint angles

Figure A.1: Sine Sweep Frequency for an Adaptive Controller

Appendix B

Interaction between J1 & J2

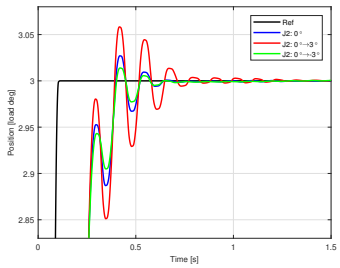

(a) J1 Motor (3°) Affected by J2 Movement

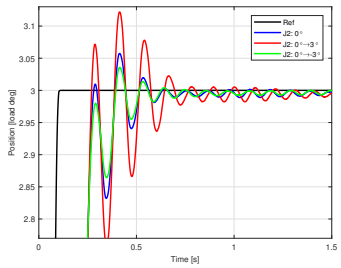

(b) J1 Load (3°) Affected by J2 Movement

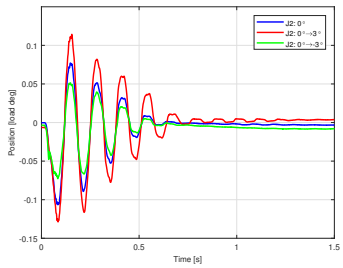

(c) J1 Torque (3°) Affected by J2 Movement

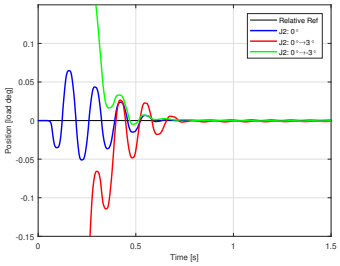

(d) J2 Motor Affected by J1 Movement (3°)

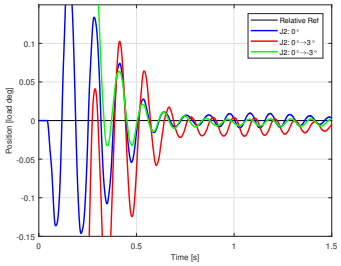

(e) J2 Load Affected by J1 Movement (3°)

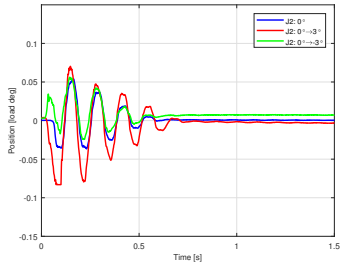

(f) J2 Torque Affected by J1 Movement (3°)

Figure B.1: Semiclosed 1DOF. J1 moves to 3°, J2 moves to [0, +3, -3][°] respectively

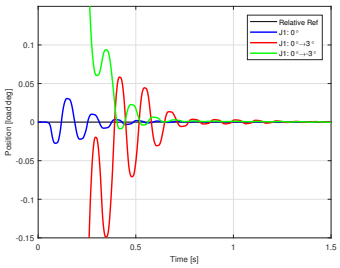

(a) J1 Motor Affected by J2 Movement (3°)

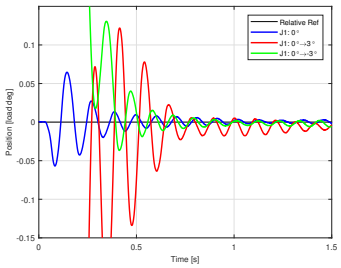

(b) J1 Load Affected by J2 Movement (3°)

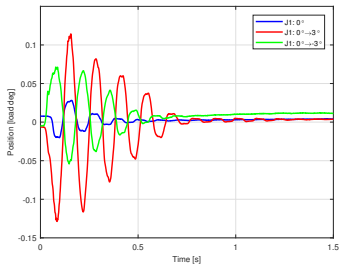

(c) J1 Torque Affected by J2 Movement (3°)

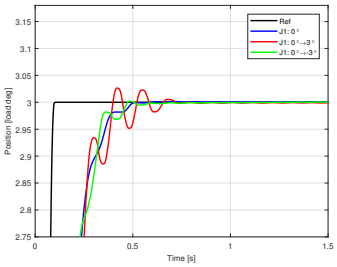

(d) J2 Motor (3°) Affected by J1 Movement

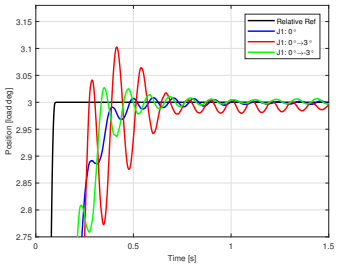

(e) J2 Load (3°) Affected by J1 Movement

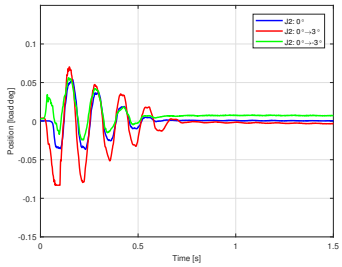

(f) J2 Torque (3°) Affected by J1 Movement

Figure B.2: Semiclosed 1DOF. J2 moves to 3°, J1 moves to [0, +3, -3][°] respectively

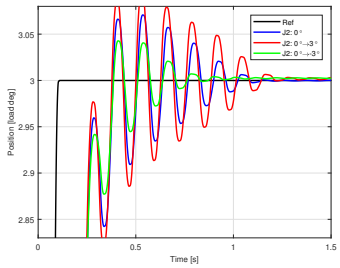

(a) J1 Motor (3°) Affected by J2 Movement

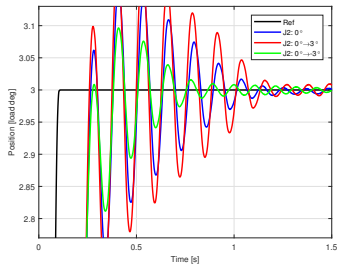

(b) J1 Load (3°) Affected by J2 Movement

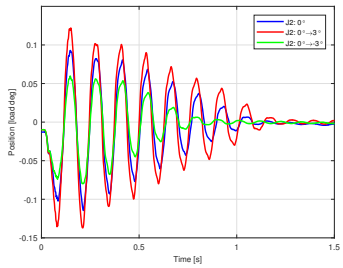

(c) J1 Torque (3°) Affected by J2 Movement

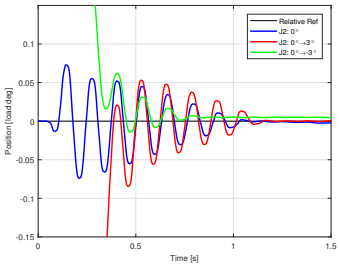

(d) J2 Motor Affected by J1 Movement (3°)

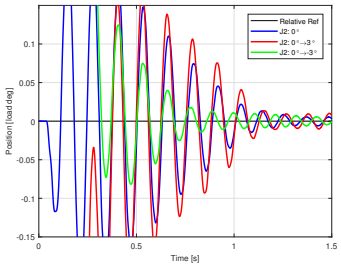

(e) J2 Load Affected by J1 Movement (3°)

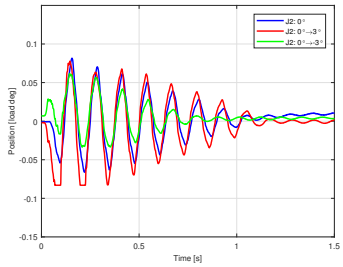

(f) J2 Torque Affected by J1 Movement (3°)

Figure B.3: Fullclosed 1DOF. J1 moves to 3°, J2 moves to [0, +3, -3][°] respectively

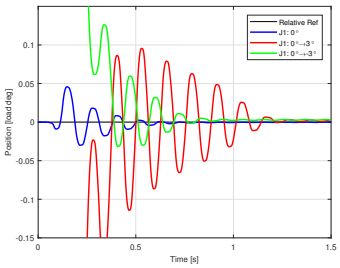

(a) J1 Motor Affected by J2 Movement (3°)

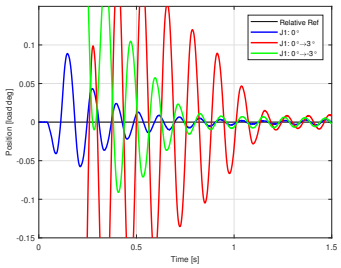

(b) J1 Load Affected by J2 Movement (3°)

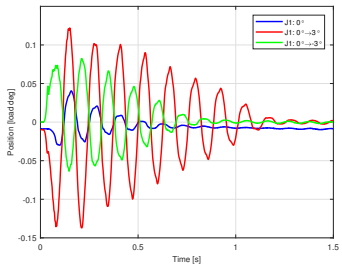

(c) J1 Torque Affected by J2 Movement (3°)

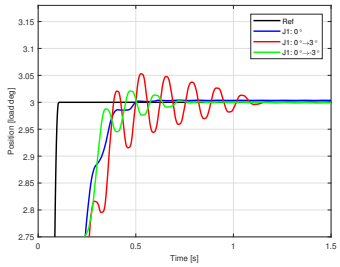

(d) J2 Motor (3°) Affected by J1 Movement

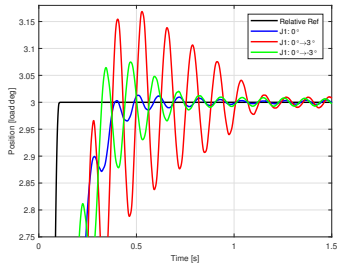

(e) J2 Load (3°) Affected by J1 Movement

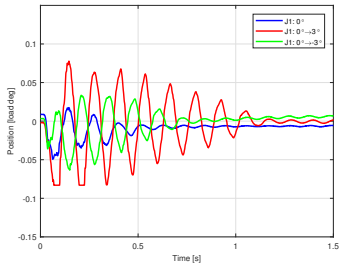

(f) J2 Torque (3°) Affected by J1 Movement

Figure B.4: Fullclosed 1DOF. J2 moves to 3°, J1 moves to [0, +3, -3][°] respectively

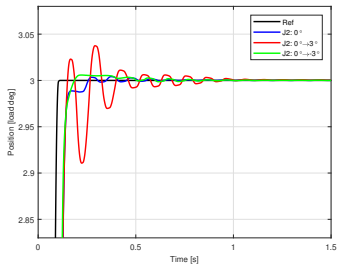

(a) J1 Motor (3°) Affected by J2 Movement

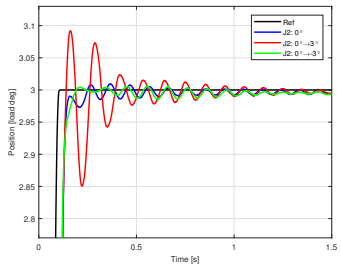

(b) J1 Load (3°) Affected by J2 Movement

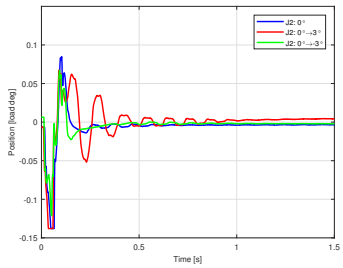

(c) J1 Torque (3°) Affected by J2 Movement

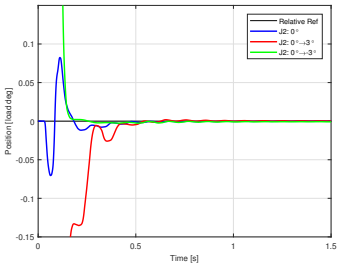

(d) J2 Motor Affected by J1 Movement (3°)

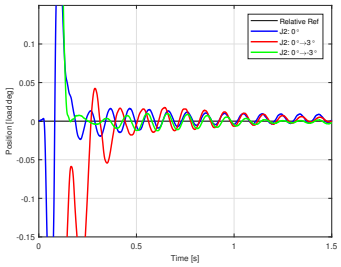

(e) J2 Load Affected by J1 Movement (3°)

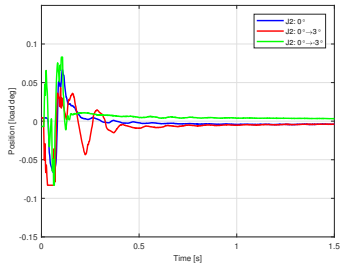

(f) J2 Torque Affected by J1 Movement (3°)

Figure B.5: Semiclosed 2DOF. J1 moves to 3°, J2 moves to [0, +3, -3][°] respectively

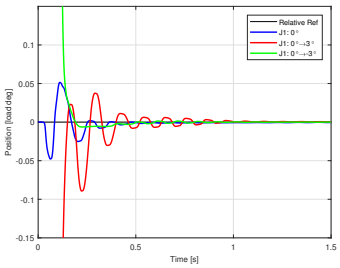

(a) J1 Motor Affected by J2 Movement (3°)

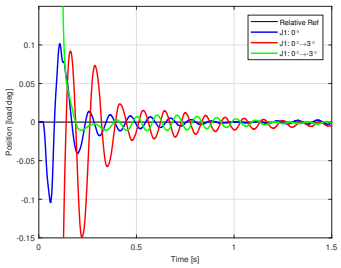

(b) J1 Load Affected by J2 Movement (3°)

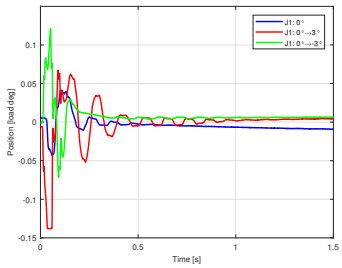

(c) J1 Torque Affected by J2 Movement (3°)

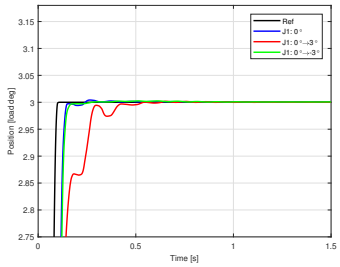

(d) J2 Motor (3°) Affected by J1 Movement

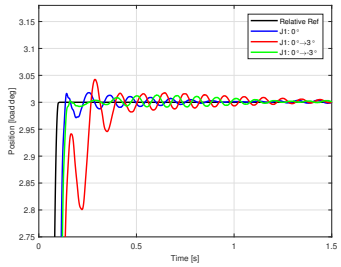

(e) J2 Load (3°) Affected by J1 Movement

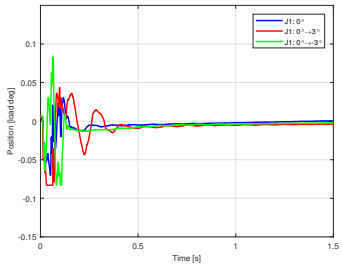

(f) J2 Torque (3°) Affected by J1 Movement

Figure B.6: Semiclosed 2DOF. J2 moves to 3°, J1 moves to [0, +3, -3][°] respectively

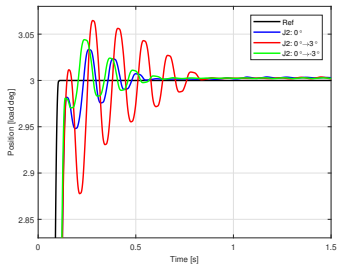

(a) J1 Motor (3°) Affected by J2 Movement

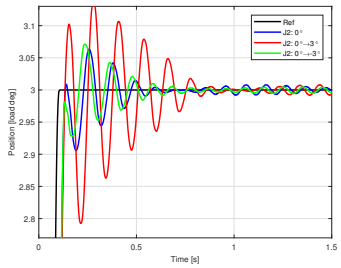

(b) J1 Load (3°) Affected by J2 Movement

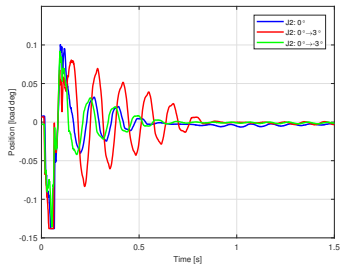

(c) J1 Torque (3°) Affected by J2 Movement

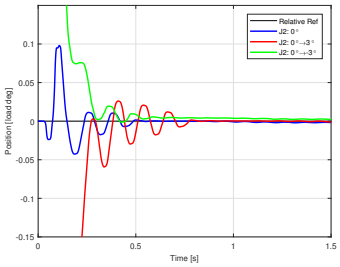

(d) J2 Motor Affected by J1 Movement (3°)

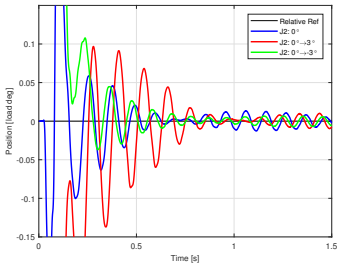

(e) J2 Load Affected by J1 Movement (3°)

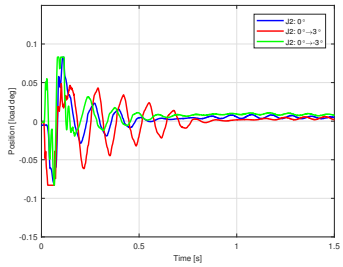

(f) J2 Torque Affected by J1 Movement (3°)

Figure B.7: Fullclosed 2DOF. J1 moves to 3°, J2 moves to [0, +3, -3][°] respectively

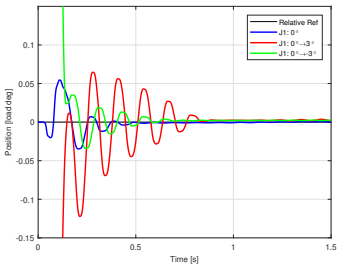

(a) J1 Motor Affected by J2 Movement (3°)

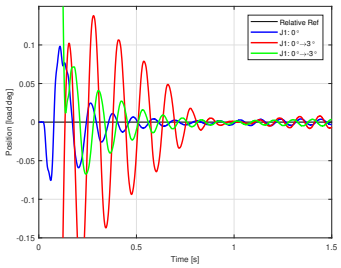

(b) J1 Load Affected by J2 Movement (3°)

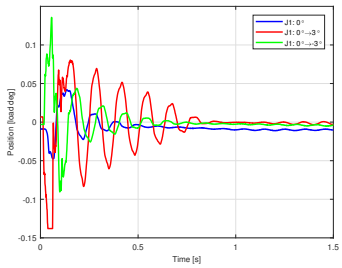

(c) J1 Torque Affected by J2 Movement (3°)

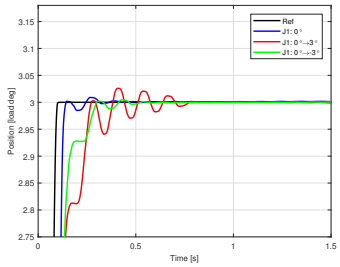

(d) J2 Motor (3°) Affected by J1 Movement

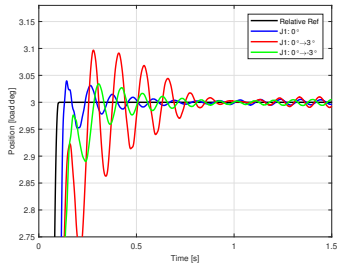

(e) J2 Load (3°) Affected by J1 Movement

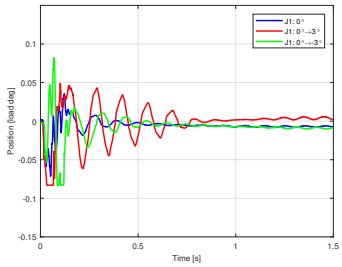

(f) J2 Torque (3°) Affected by J1 Movement

Figure B.8: Fullclosed 2DOF. J2 moves to 3°, J1 moves to [0, +3, -3][°] respectively

Appendix C

Flowchart to design a controller based in the root locus

Figure C.1 shows the flowchart to design a controller based in the root locus.

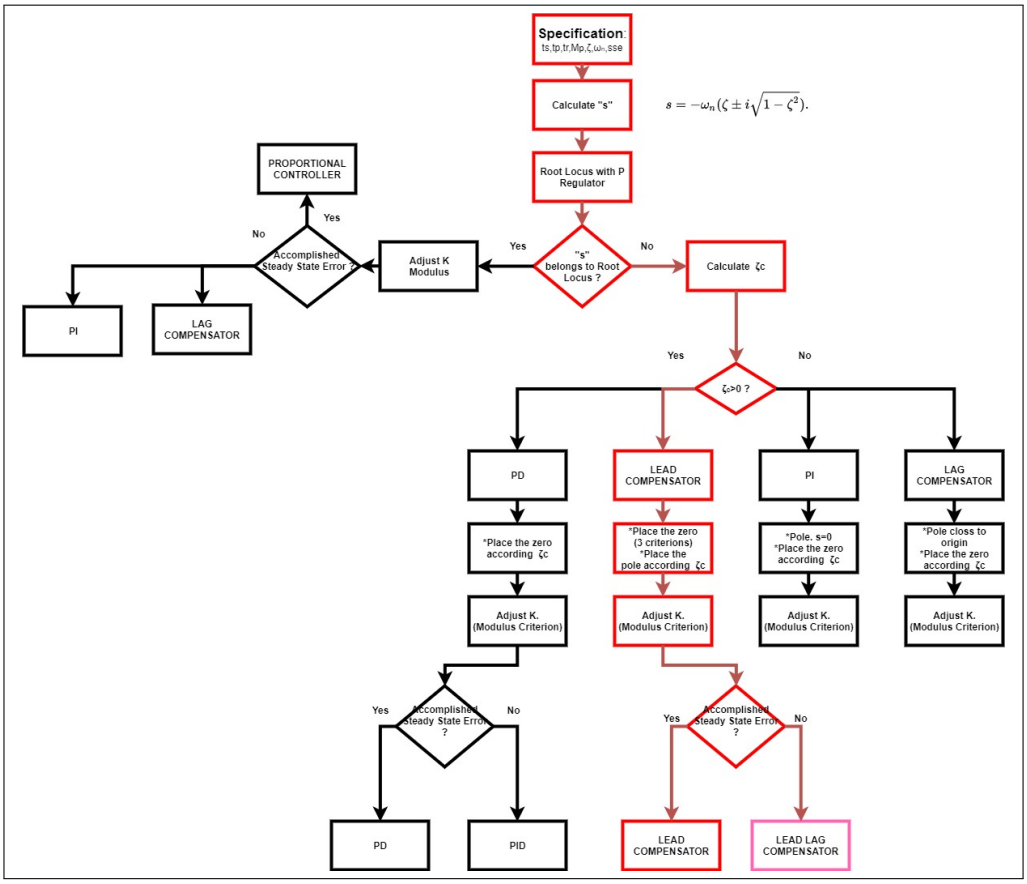

Figure C.1: Flowchart to design a controller